Voltage Support Capacity Improvement for Wind Farms with Reactive Power Substitution Control

Yuegong Li, *Student Member*, *IEEE*, Guorong Zhu, *Senior Member*, *IEEE*, Jianghua Lu, *Member*, *IEEE*, *Member*, *CSEE*, and Hua Geng, *Fellow*, *IEEE*

***Abstract*—Generally, voltage support at the point of common coupling (PCC) of a wind farm is achieved through centralized static var generators (SVGs). Since the reactive power requirements occupy their capacity in a steady state, the reactive power support capacity of the SVG is limited during high voltage ride through (HVRT) or low voltage ride through (LVRT). While wind turbines can provide voltage support in accordance with the grid code, their responses are usually delayed due to communication and transmission lags. To enhance the dynamic performance of wind farms during fault ride-through, a reactive power substitution (RPS) control strategy is proposed in this paper. In a steady state, this RPS control method preferentially utilizes the remaining capacity of wind turbines to substitute for the output of the SVG. Considering differences in terminal voltage characteristics and operating conditions, this RPS control method employs a particle swarm optimization (PSO) algorithm to ensure that wind turbines can provide their optimal reactive power support capacity. When the grid voltage swells or drops, the SVG has a sufficient reactive power reserve to support the grid quickly. This paper utilizes a regional power grid incorporating two wind farms connected to different buses as a case study to validate this RPS control strategy.**

***Index Terms*—Active voltage support, high voltage ride-through, large-scale wind farm control, low voltage ride-through, reactive power substitution, wind turbine.**

I. INTRODUCTION

MORE and more large-scale wind farms are connected to power systems, and their penetration rates in new power systems are increasing [1]. Grid disturbances, as well as the randomness and fluctuation of wind speed cause severe voltage fluctuations for wind farms [2]. In particular, when the grid voltage swells or drops, the grid code require renewable energy stations to support the grid voltage promptly while maintaining grid-connected operation [3], [4]. According to the grid code of China, Table I gives the reactive current that wind farms need to provide to the grid during HVRT or LVRT. If the wind farm is disconnected from the grid after experiencing a large disturbance, the secure and stable operation of the regional power system may be affected [5]. Therefore, enhancing the voltage support capacity during fault ride-through for large-scale wind farms has become a significant concern.

There are many types of control structures for large-scale wind farms, such as centralized control, distributed control, decentralized control, and hierarchical control [6]–[8]. Due to promised performance in global optimization and control, a centralized control structure is widely adopted [7]. Generally, a wind farm in the centralized control mode will install large-capacity reactive power compensators at the point of common coupling (PCC). These common facilities can be Static Var Generators (SVGs), Synchronous Condensers (SCs), or others [9]–[11]. Conventionally, wind turbines operate in the Maximum Power Point Tracking (MPPT) mode in a steady state. This working mode can maximize the active power output. However, the voltage support function of wind farms is mainly borne by SVGs at this time [12], [13]. When the grid voltage suddenly swells or drops, the remaining capacity of SVGs may not provide adequate reactive power support. An effective method is to expand the rated capacity of these reactive power compensators, but this is costly.

Except for separate reactive power compensators, wind turbines can also be utilized to play a vital role in supporting the grid voltage. The distribution of wind turbines is relatively scattered. This distribution pattern determines that their operating states and reactive power support capacity are different. Then, the coupling factor between wind turbines should also be considered. Some other studies focus on the cooperative control of wind turbines during HVRT or LVRT. In [14] and [15], the collaborative control strategies between wind turbines based on an optimization algorithm are proposed during LVRT. In [16] and [17], model predictive control (MPC) methods are designed to get the control command of each piece of equipment during HVRT. The commonality of these control strategies is to address collaborative issues between wind turbines by constructing optimization models. According to the operation data sent by wind turbines, the central controller of a wind farm generates a control command for wind turbines by solving complex optimization problems. The time to solve such control command will increase with the growth of the wind farm scale. Besides, both voltage sampling

---

Manuscript received September 23, 2024; revised November 19, 2024; accepted December 23, 2024. Date of online publication May 16, 2025; date of current version May 21, 2025. This work was supported in part by the National Natural Science Foundation of China under Grant U2166601 and 51977163.

Y. G. Li and G. R. Zhu are with the School of Automation, Wuhan University of Technology, Wuhan 430070, China. G. R. Zhu is also with the State Key Laboratory of Maritime Technology and Safety, Wuhan University of Technology, Wuhan 430063, China.

J. H. Lu is with the College of Information Science and Engineering, Wuhan University of Science and Technology, Wuhan 430081, China.

H. Geng (corresponding author, email: genghua@tsinghua.edu.cn) is with the Department of Automation, Tsinghua University, Beijing 100084, China.

DOI: 10.17775/CSEEJPES.2024.07190

TABLE I
REQUIREMENTS FOR REACTIVE CURRENT BASED ON GRID CODE OF CHINA

Voltage at PCC (p.u)	Operating status	Requirements for reactive current		
		Symmetrical fault	Asymmetric fault	
			Positive sequence	Negative sequence
<0.2	Off-grid	–	–	–
[0.2 0.9)	LVRT	$K_1(0.9-U)I_N$[a]	$K_{2+}(0.9-U^+)I_N$[b]	$K_{2-}(0.9-U^-)$[c]
[0.9 1.1]	Normal	–	–	–
(1.1 1.3]	HVRT	$K_3(U-1.1)I_N$[d]	–	–
>1.3	Off-grid	–	–	–

[a] U is the voltage at PCC of the wind farm, measured in unit (p.u). I_N is the rated current of the wind farm, measured in amperes (A). K_1 is the gain coefficient, and its value range should not be less than 1.5, preferably not greater than 3.

[b] U^+ is the positive sequence component of U, measured in unit (p.u). K_{2+} is the gain coefficient of positive sequence reactive current, and its value range should be bigger than 1.

[c] U^- is the negative sequence component of U, measured in unit (p.u). K_{2-} is the gain coefficient of negative sequence reactive current, and its value range should be bigger than 1.

[d] K_3 is the gain coefficient, and its value range should be bigger than 3.

and information transmission are time-consuming. Due to the impedance between wind turbines and SVGs, there is a delay in reactive power transmission. These factors may prevent wind turbines from providing reactive power support in time.

For a wind farm operating under a centralized control mode, the greater the reactive power reserve available in a steady state, the more effectively it can support the voltage during LVRT or HVRT. This key issue is to increase the reactive power reserve of a wind farm without adding any hardware cost. Then, an effective way to address this problem is to minimize the output of the SVG. However, the remaining capacity of a wind turbine in a steady state is not fully utilized by conventional methods.

Accordingly, a reactive power substitution (RPS) control strategy is designed to enhance the dynamic performance of a wind farm during LVRT or HVRT in this paper. Under this RPS control method, the remaining capacity of a wind turbine is preferentially utilized to substitute for the output of the SVG in a steady state. To limit the deviation of the terminal voltage to the specified threshold, this RPS method employs an intelligence algorithm to adjust the operating state of each wind turbine. The feasibility of this RPS control method is verified using a regional power grid that includes two wind farms located at different buses during HVRT or LVRT. The main contributions of this article are reflected in two aspects: 1) The reactive support characteristics of wind turbines and SVGs are analyzed in detail. An SVG with a large capacity is more suitable for providing a sufficient reactive current. 2) An RPS control strategy is proposed. This control strategy only changes the reactive power distribution within the wind farm in a steady state. Its effectiveness has been verified with different power systems.

The rest of this paper is organized as follows. Section II analyzes the reactive power characteristics of a wind farm during HVRT and LVRT. In this Section, the topology and modeling of a wind farm is also outlined. Section III proposes and analyzes this RPS control strategy. Two case studies and their simulation results are given in Section IV. Section V summarizes the major conclusion of this paper.

II. MODELING AND ANALYSIS OF WIND FARMS

Figure 1(a) presents the typical topology of a radial PMSG-based (Permanent Magnet Synchronous Generator) wind farm. Obviously, there are many wind turbines connected to a feeder line. Each wind turbine injects its active and reactive power through a 0.69 kV/35 kV transformer. Besides, SVGs have been deployed at the PCC to provide voltage support. Fig. 1(b) gives the structure of a conventional centralized control mode employed by a large-scale wind farm. Under this control mode, wind turbines will only respond to control commands received from the central controller in normal operation. Since this paper focuses exclusively on variations of dynamic performance between wind turbines and SVGs during HVRT and LVRT, the control strategy for these facilities in a steady state is no longer described.

A. Control Strategy for Wind Turbines and SVGs During HVRT and LVRT

Usually, the control strategy for wind turbines during HVRT or LVRT consists of three stages: the initial stage, duration stage, and post-event voltage recovery stage. At the initial stage, the chopper circuit consumes excess active power to keep V_{dc} within the threshold. During the duration stage, the facilities within the wind farm are required to provide voltage support. Fig. 2 presents the modified current control strategy for wind turbines during HVRT and LVRT. $I_{\mathrm{d\_ref}}$ and $I_{\mathrm{q\_ref}}$ are the references for the wind turbine, respectively. $I_{\mathrm{q\_norm}}$ is the q-axis current during the pre-event period. The voltage-oriented current vector control method based on a phase-locked loop (PLL) is employed to realize a decoupling control strategy for the inner-loop current. In this stage, the reactive current offered by the wind turbine has to meet the following conditions:

$$\Delta I_{\mathrm{qref}} = \begin{cases} K_{\mathrm{LVRT}}(V_{\mathrm{LVRT}}-V_{\mathrm{WT}})I_N, & (0.2 \le V_{\mathrm{WT}} \le 0.9) \\ K_{\mathrm{HVRT}}(V_{\mathrm{pcc}}-V_{\mathrm{WT}})I_N, & (1.1 \le V_{\mathrm{WT}} \le 1.3) \end{cases} \tag{1}$$

where V_{WT} and I_N are the terminal voltage and rated current of the wind turbine. V_{LVRT} and V_{HVRT} indicate the voltage boundaries based on the grid code. K_{LVRT} and K_{HVRT} are the gain coefficients. During HVRT or LVRT, the wind turbine outputs reactive current in priority. When the voltage at PCC returns to normal, the wind turbine should be restored to the

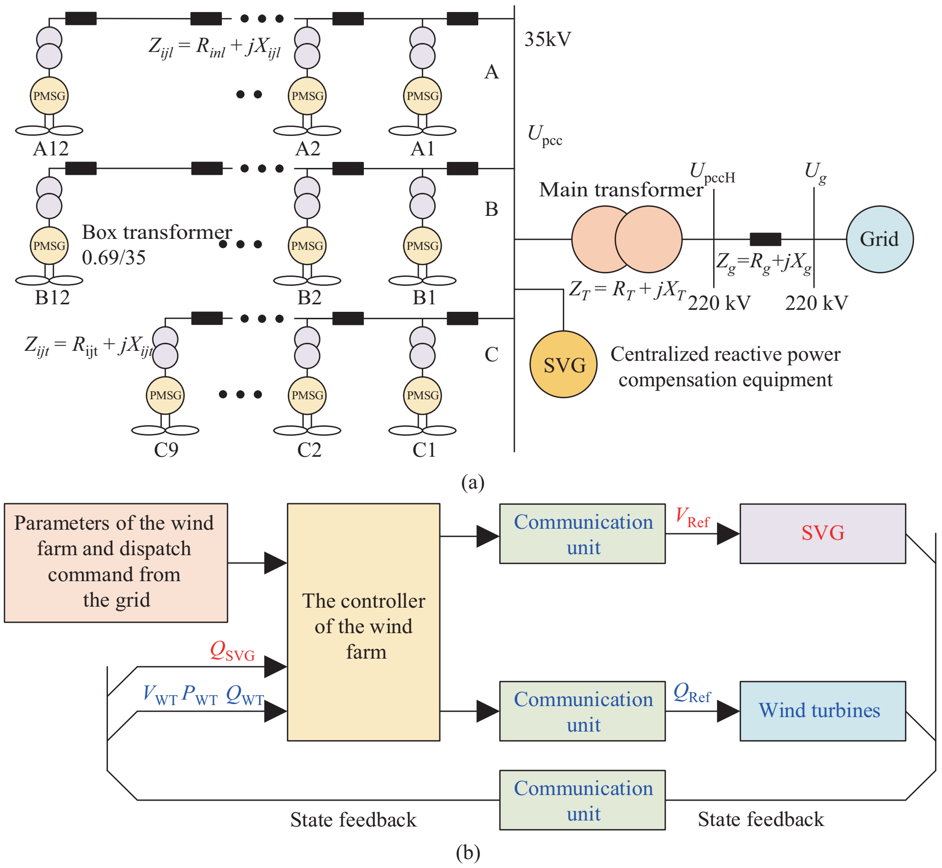

Fig. 1. Overview of a typical radiative wind farm based on the centralized control mode. (a) Topology. (b) Structure of the centralized control mode.

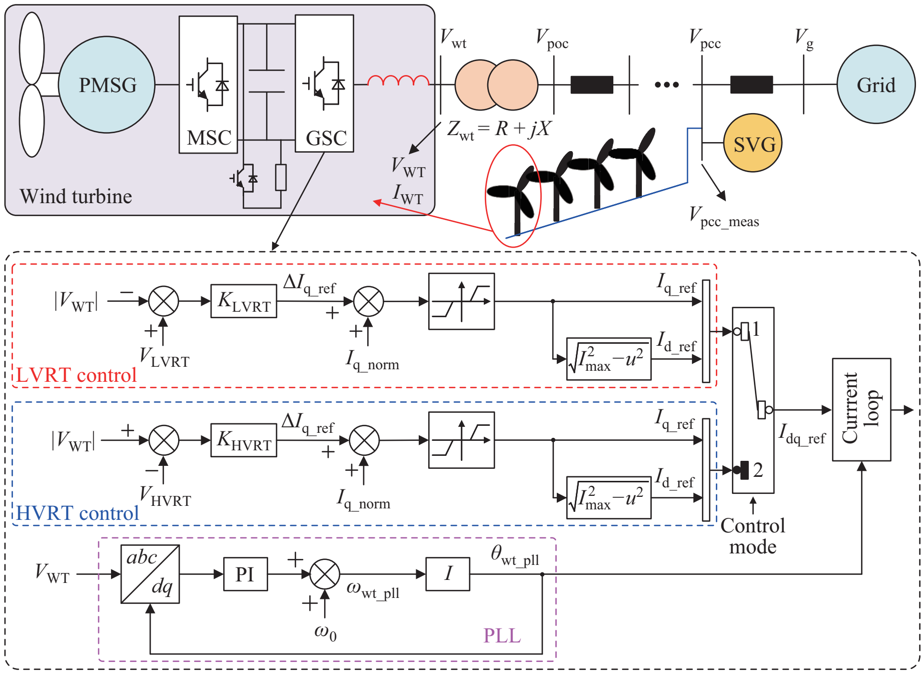

Fig. 2. Current control strategy of a wind turbine during HVRT and LVRT.

pre-event operating state within a specified time. The control strategy for the inner current loop shown in Fig. 2 is different from the conventional method. I_{q_ref} includes two aspects. One is the reactive current increment provided by the wind turbine. The other is the reactive current in the pre-event period.

The control strategy for the inner-loop current of the SVG is analogous to that employed in wind turbines. Besides, SVG has a large capacity and does not generate active power. Given that the output of the SVG is significantly greater than its active power loss, this paper assumes that the output of the SVG can achieve its rated capacity.

B. Modeling of a Wind Farm in Different Frames

A feeder line within a wind farm connects multiple wind turbines and their operating states will affect those of others and the SVG. Assuming that the SVG has enough reactive power, it can achieve a constant voltage at PCC. The interaction between wind turbines in different feeder lines is weaker than that in the same feeder line. Therefore, a simplified model is built to visually illustrate this interaction in this paper, as shown in Fig. 3(a). This model contains three wind turbines and one SVG in the same feeder line in Fig. 3(a). $\boldsymbol{V}_g$, $\boldsymbol{V}_{\mathrm{pcc}}$ and $\boldsymbol{V}_{\mathrm{WT}i}$ are the grid voltage, the voltage at PCC and the terminal voltage of the No.ith wind turbine, respectively. $Z_{\mathrm{WT}i}$, Z_{Ti} and Z_g are the impedance of the feeder line, the impedance of the box transformer and the equivalent impedance from PCC to the grid, respectively.

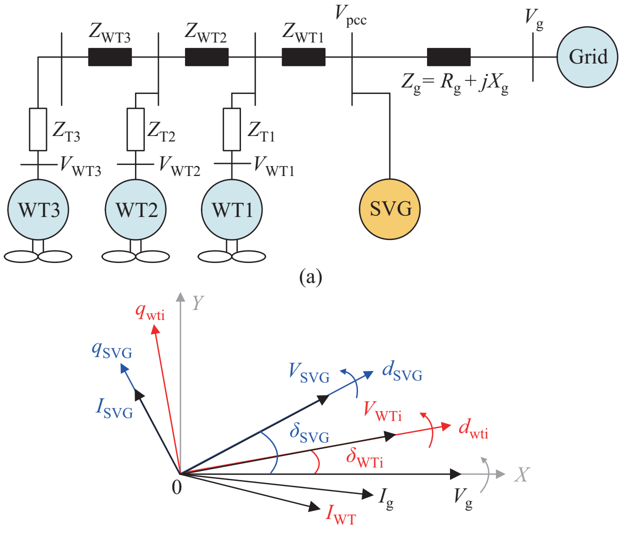

Fig. 3. Structure and different rotation frames of a wind farm. (a) The model. (b) Different rotation frames.

In Fig. 3(a), this paper defines that the grid provides a phase reference. The PLLs of the SVG and wind turbines will synchronize with the grid voltage vector. Accordingly, as shown in Fig. 3(b), this paper sets three rotation frames for different types of facilities. The rotation frame of the grid voltage vector is defined as the XY frame, and its angular frequency is ω_g. The dq_{SVG} frame is represented with the PLL of the SVG, and its voltage vector at PCC is ω_{SVG}. The PLL of each wind turbine is defined as the $dq_{\mathrm{WT}i}$ frame, and its angular frequency is $\omega_{\mathrm{WT}i}$.

Generally, ω_g is regarded as a constant value. Both the wind turbines and the SVG adopt a grid-following control method. Thus, their PLLs remain synchronized with the grid. Their grid-side converters can be simplified to controlled current sources during HVRT or LVRT [18], [19]. Similarly, the grid is equivalent to an independent voltage source. Fig. 4 gives the simplified models of this wind farm under different frames. The phase angle of the voltage vector in each rotation frame is different, but their amplitudes can remain constant. The transformation of current vectors is similar.

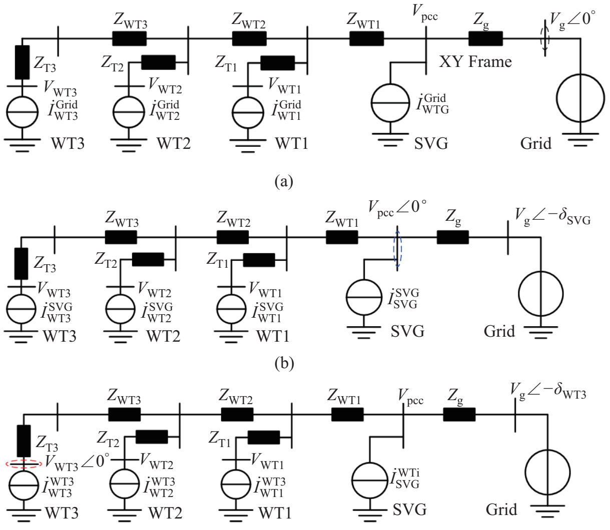

Fig. 4. A simplified model of a wind farm in different rotation frames. (a) XY frame. (b) dq_{SVG} frame. (c) $dq_{\mathrm{WT}i}$ frame.

For example, $\dot{I}_{\mathrm{WT}i}^{\mathrm{WTi}}$ and $\dot{I}_{\mathrm{SVG}}^{\mathrm{SVG}}$ are the current phasors in their own dq rotation frame. $\delta_{\mathrm{WT}i}$ and δ_{SVG} are the outputs of PLLs. When the $dq_{\mathrm{WT}i}$ rotation frame is selected as the reference rotation frame, the $\dot{I}_{\mathrm{SVG}}^{\mathrm{SVG}}$ will be converted into $\dot{I}_{\mathrm{SVG}}^{\mathrm{WTi}}$ through coordinate transformation. Conversely, when the dq_{SVG} rotation frame is employed as the reference rotation frame, $\dot{I}_{\mathrm{WT}i}^{\mathrm{WTi}}$ has to be converted into $\dot{I}_{\mathrm{WT}i}^{\mathrm{SVG}}$. This transformation method is:

$$\left\{\begin{aligned} \dot{I}_{\mathrm{SVG}}^{\mathrm{WTi}} &= e^{j(\delta_{\mathrm{SVG}}-\delta_{\mathrm{WT}i})}\dot{I}_{\mathrm{SVG}}^{\mathrm{SVG}} \\ \dot{I}_{\mathrm{WT}i}^{\mathrm{SVG}} &= e^{j(\delta_{\mathrm{WT}i}-\delta_{\mathrm{SVG}})}\dot{I}_{\mathrm{WT}i}^{\mathrm{WTi}} \end{aligned}\right. \tag{2}$$

According to Fig. 4, $\boldsymbol{V}_{\mathrm{WTi}}$ can be expressed as:

$$\begin{aligned} \dot{V}_{\mathrm{WT}i} = V_g\angle-\delta_{\mathrm{WT}i} + Z_g\left(\dot{I}_{\mathrm{SVG}}^{\mathrm{WTi}} + \sum_{1}^{N}\dot{I}_{\mathrm{WTk}}^{\mathrm{WTi}}\right) \\ + \sum_{1}^{i}\left(Z_{\mathrm{WTk}}\sum_{1}^{N-1}\dot{I}_{\mathrm{WTk}}^{\mathrm{WTi}}\right) + Z_{\mathrm{Ti}}\dot{I}_{\mathrm{WT}i}^{\mathrm{WTi}} \end{aligned} \tag{3}$$

Decomposing (3) into the $dq_{\mathrm{WT}i}$ rotation frame, the voltage components of $\dot{V}_{\mathrm{WT}i}^{\mathrm{WTi}}$ in dq-axis are given by (4).

$$\left\{\begin{aligned} V_{\mathrm{WTi\_d}} = V_g\cos(-\delta_{\mathrm{WT}i}) + \mathrm{Re}\Big[\Big(Z_g + \textstyle\sum_1^N Z_{\mathrm{WTk}} + Z_{\mathrm{Ti}}\Big) \\ \dot{I}_{\mathrm{WT}i}^{\mathrm{WTi}} + \textstyle\sum_1^{i-1}\dot{I}_{\mathrm{WTk}}^{\mathrm{WTi}}\Big(\textstyle\sum_1^{N-1} Z_{\mathrm{WTm}} + Z_g\Big) + Z_g\dot{I}_{\mathrm{SVG}}^{\mathrm{WTi}}\Big] \\ V_{\mathrm{WTi\_q}} = V_g\sin(-\delta_{\mathrm{WT}i}) + \mathrm{Im}\Big[\Big(Z_g + \textstyle\sum_1^i Z_{\mathrm{WTk}} + Z_{\mathrm{Ti}}\Big) \\ \dot{I}_{\mathrm{WT}i}^{\mathrm{WTi}} + \textstyle\sum_1^{i-1}\dot{I}_{\mathrm{WTk}}^{\mathrm{WTi}}\Big(\textstyle\sum_1^{N-1} Z_{\mathrm{WTm}} + Z_g\Big) + Z_g\dot{I}_{\mathrm{SVG}}^{\mathrm{WTi}}\Big] \end{aligned}\right. \tag{4}$$

Similarly, the voltage at PCC and its dq-axis components under the dq_{SVG} rotation frame are given in (5) and (6), respectively.

$$\dot{V}_{\mathrm{pcc}} = V_g\angle-\delta_{\mathrm{SVG}} + Z_g\left(\dot{I}_{\mathrm{SVG}}^{\mathrm{SVG}} + \sum_{1}^{N}\dot{I}_{\mathrm{WT}i}^{\mathrm{SVG}}\right) \tag{5}$$

$$\begin{cases} V_{\mathrm{pcc\_d}} = V_g\cos(-\delta_{\mathrm{SVG}}) + \mathrm{Re}\left[Z_g\dot{I}_{\mathrm{SVG}}^{\mathrm{SVG}} + Z_g\sum_{1}^{N}\dot{I}_{\mathrm{WT}i}^{\mathrm{SVG}}\right] \\ V_{\mathrm{pcc\_q}} = V_g\sin(-\delta_{\mathrm{SVG}}) + \mathrm{Im}\left[Z_g\dot{I}_{\mathrm{SVG}}^{\mathrm{SVG}} + Z_g\sum_{1}^{N}\dot{I}_{\mathrm{WT}i}^{\mathrm{SVG}}\right] \end{cases} \tag{6}$$

When (2) to (6) are combined, the simplified system model of this wind farm is given in Fig. 5. This model diagram describes the impact of the operating states of the primary facilities on $\boldsymbol{V}_{\mathrm{pcc}}$ and $\boldsymbol{V}_{\mathrm{WTi}}$. The main factor affecting the amplitude of $\boldsymbol{V}_{\mathrm{pcc}}$ is the output of the SVG. Moreover, the amplitude of $\boldsymbol{V}_{\mathrm{WTi}}$ is determined by the wind turbine. Although both $\boldsymbol{V}_{\mathrm{pcc}}$ and $\boldsymbol{V}_{\mathrm{WTi}}$ are affected by the injected reactive power, it is necessary to find out the impact of the reactive reserve on the voltage support capacity based on the topology of the power system expressed in Fig. 3(a).

C. Analysis of Reactive Power Support Characteristics

The voltage amplitude calculation of each wind turbine has to get the phase angle output by its PLL. A high-order nonlinear equation consists of (4) to (6). Since this calculation process needs to solve high-dimensional nonlinear equations, it is difficult to obtain the accurate values of these angles. However, an ODE solver in MATLAB is used to obtain the time-domain dynamic trajectories of $\boldsymbol{V}_{\mathrm{pcc}}$ and $\boldsymbol{V}_{\mathrm{WTi}}$. To clearly illustrate the impact of the SVG operating state and further analyze the coupling phenomenon during the process of fault ride-through, this paper defines two operating states to explain the effect on the dynamic processes of key nodes under different operating states of the SVG. In both cases, $\boldsymbol{V}_{\mathrm{pcc}}$ is regulated to 1.0 p.u. by SVG.

1) Case A

To simplify the analysis, each wind turbine only outputs the same active power and its operating state is $(I_{\mathrm{d_ref}}+\mathrm{j}I_{\mathrm{q_ref}}) = (0.64\,+\,\mathrm{j}0)$p.u. Similarly, the SVG meet the full reactive power requirement of the wind farm and its operating state is $I_{\mathrm{q\_SVG}} = 0.88$ p.u.

2) Case B:

Similarly, the operating state of each wind turbine is the same. The reactive power requirement is jointly met by the wind turbines. In addition, the initial current of each wind turbine is $(I_{\mathrm{d\_ref}}+\mathrm{j}I_{\mathrm{q\_ref}}) = (0.64-\mathrm{j}0.18)$ p.u. and the initial operating state of the SVG is $(I_{\mathrm{d\_SVG}}+\mathrm{j}I_{\mathrm{q\_SVG}}) = (0+\mathrm{j}0.02)$ p.u.

At $t_0 = 10$ s, V_g is set to 0.6 p.u. to obtain the dynamic response characteristics in different cases. After 0.5 s, the voltage returns to normal. The dynamic response processes of $\boldsymbol{V}_{\mathrm{pcc}}$ and $\boldsymbol{V}_{\mathrm{WTi}}$ are shown in Fig. 6. Since the output reactive power of the SVG is less under normal operation in Case B, the SVG can provide faster reactive power within a shorter time during LVRT. In Case B, the drop rate of $\boldsymbol{V}_{\mathrm{pcc}}$ is 3.42 p.u./s and that of $\boldsymbol{V}_{\mathrm{WTi}}$ is 2.86 p.u./s. Compared to the time-domain trajectories of $\boldsymbol{V}_{\mathrm{pcc}}$ and $\boldsymbol{V}_{\mathrm{WTi}}$ in different cases, the drop rates of both voltages are lower when the wind turbines finish reactive power output before the LVRT period. Additionally, $I_{\mathrm{q\_pcc}}$ in Case B is 0.77 p.u. Therefore, the minimum value of the terminal voltage has also increased. Similarly, in Fig. 6(c), due to the fact that wind turbines provide a greater reactive current, the terminal voltages of the other two wind turbines have also increased.

It should be pointed out that the dq-axis current component at PCC of the wind farm will not change regardless of whether

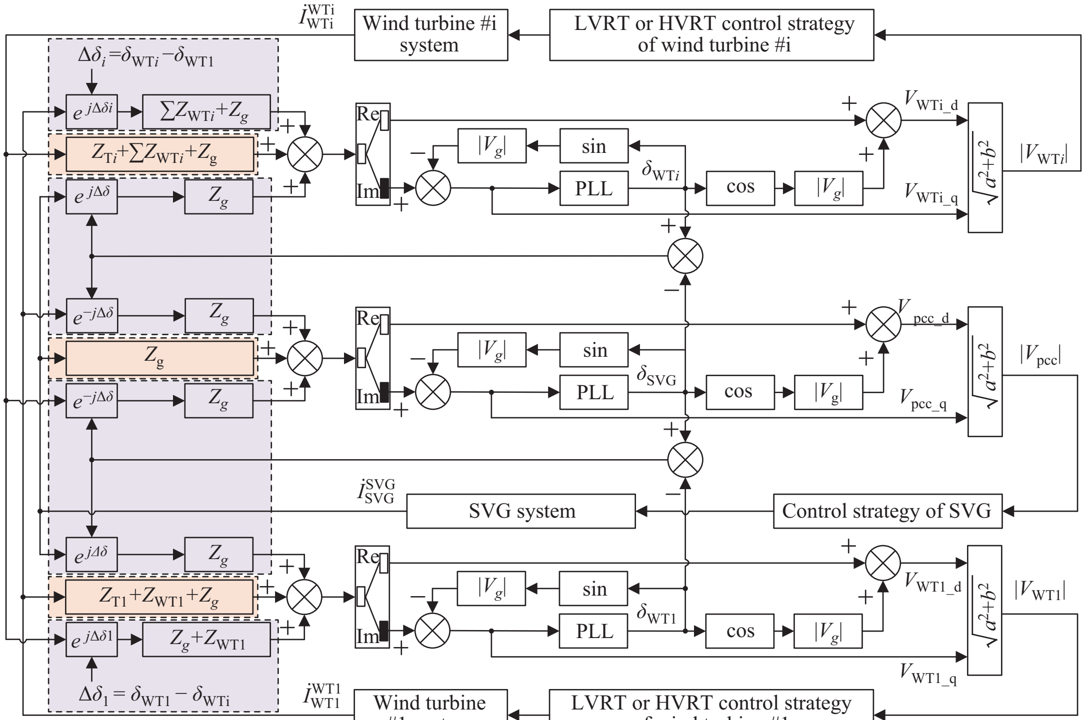

Fig. 5. Model diagram of a simplified wind farm system.

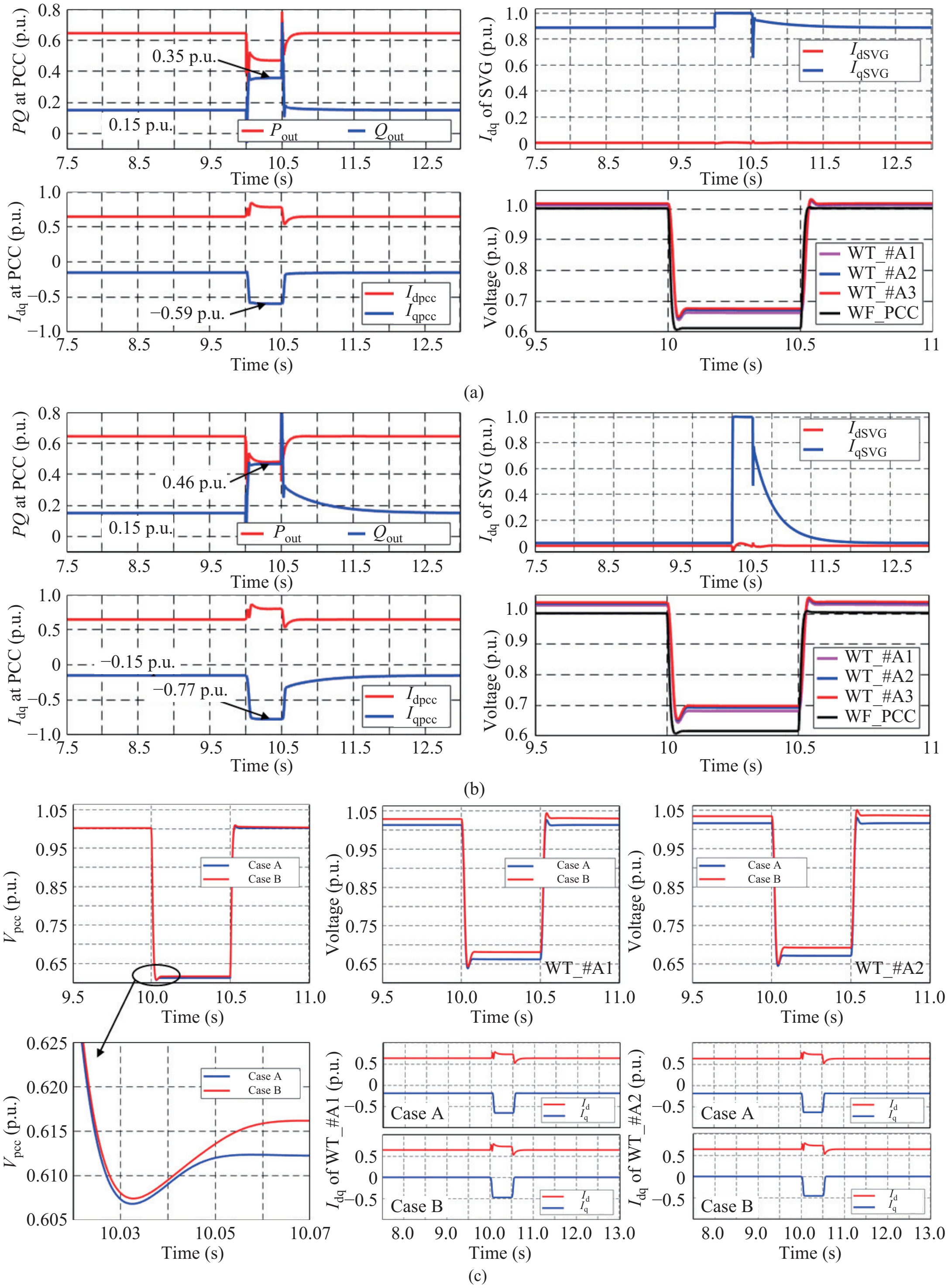

(a)

(b)

(c)

Fig. 6. Dynamic processes under (a) Case A and (b) Case B during LVRT, and (c) the comparison of terminal voltages.

the output of the SVG is close to zero. In other words, when the wind turbines provide reactive power, only the reactive power distribution inside the wind farm is changed. In addition, compared with the conventional central control mode, the central controller no longer sends any control command to each facility during fault ride-through. The delay arising from both data communication and the solving of optimization problems will be absent.

Although the increment of current the component at PCC of the wind farm is the same during HVRT, its rate of change is different, as shown in Figs. 7(a) and 7(b). Furthermore, the reactive current increment provided by the SVG in Case A can reach 1.88 p.u. Conversely, that in Case B is only 1.02 p.u. Therefore, the voltage overshoot of $\boldsymbol{V}_{\mathrm{pcc}}$ and $\boldsymbol{V}_{\mathrm{WTi}}$ in Case A is larger than that in Case B, as shown in Fig. 7(c). However, the dynamic response process of $\boldsymbol{V}_{\mathrm{pcc}}$ and $\boldsymbol{V}_{\mathrm{WTi}}$ in Case B is better than that in Case A during the voltage recovery period.

To summarize, while both the wind turbines and the SVG can offer voltage support to the grid during fault ride-through, their characteristics in this regard differ significantly. The reasons for these differences are analyzed in detail: 1) The converter capacity of the SVG is much larger than that of a wind turbine. Despite the large number of wind turbines, their support for the grid voltage is limited due to the higher impedance of the feeder lines. 2) Regarding the speed of reactive power compensation, SVGs are centrally installed at PCC and can monitor $\boldsymbol{V}_{\mathrm{pcc}}$ in real time. When the amplitude of $\boldsymbol{V}_{\mathrm{pcc}}$ exceeds a predetermined threshold, the SVG can quickly supply reactive power support. However, the wind turbines would experience a certain lag in reactive power transmission. 3) In a steady state, the deviation of the terminal voltage tends to increase with the addition of an equivalent impedance in the feeder line, potentially surpassing the designed threshold.

III. REACTIVE POWER SUBSTITUTION CONTROL STRATEGY

A. Structure and Implementation Process of RPS

As previously analysis, an SVG with a large reactive power reserve under normal operation plays an important role during the period of HVRT or LVRT. Moreover, in a steady state, wind turbines can output reactive power to reduce the output of the SVG. Consequently, to enhance the voltage support capacity of wind farms, an RPS control method is proposed, which only adjusts the operating state of an existing wind farm without changing its hardware facilities. Figs. 8(a) and 8(b) show its structure and implementation process, respectively. According to Fig. 8(b), this RPS control method contains two stages and its implementation process is introduced as follows:

Before $t = t_0$, the wind farm works under the normal operation mode.

At $t = t_0$, the first stage of this RPS control strategy is implemented. During $[t_0 \;\; t_1]$, if Q_{SVG} remains within a certain range, the wind farm would maintain its current operating state. On the contrary, if Q_{SVG} exceeds the threshold, a control instruction will be sent to each wind turbine based on the optimization algorithm. This adjustment will minimize the output of the SVG again.

If the grid voltage swells or drops suddenly at $t = t_1$, the wind farm will enter the fault ride-through mode. It will trigger the wind farm to enter the secondary stage of this RPS control strategy. In this stage, the SVG and wind turbines will promptly provide reactive power support following their control methods. Besides, each wind turbine provides reactive power support based on its terminal voltage during HVRT/LVRT. It can reduce the delay generated by information transmission and the solving process.

After $t = t_2$, when the voltage of the power grid returns to normal, the wind farm will return to its pre-event operating state.

B. Method for Obtaining Reactive Power Command

The grid code has different response requirements for wind farms during LVRT and HVRT. In a real power grid, the voltage at PCC would swell or drop suddenly. Thus, to ensure that the wind farm has a sufficient reactive power reserve to deal with these emergencies in both cases, it should minimize the output of the SVG in a steady state, as expressed in (7).

$$\min\left\{\left|\frac{Q_{\mathrm{SVG}}}{Q_{\mathrm{SVGmax}} - Q_{\mathrm{SVGmin}}}\right|\right\} \tag{7}$$

where Q_{SVGmax} and Q_{SVGmin} are the upper and lower thresholds. To achieve this objective, the participation of the wind turbines is required. However, due to the impedances of the feeder lines and the box transformer, their terminal voltage deviations may exceed the threshold, especially for the wind turbines at the end of the feeder lines [20]. Therefore, the other objective is to restrict the terminal voltage deviation, as shown in (8).

$$\min\left\{\frac{1}{N_{\mathrm{WT}}}\sum_{i=1}^{m}\sum_{j=1}^{n}\left(\frac{V_{\mathrm{WT}ij} - V_{\mathrm{N}ij}}{V_{\mathrm{N}ij}}\right)^2\right\} \tag{8}$$

where $V_{\mathrm{WT}ii}$ and $V_{\mathrm{N}ij}$ are the terminal and rated voltages of each wind turbine, respectively. Its location is represented as $[m, n]$. In summary, the optimization objective of this RPS control strategy in a steady state contains two components: minimizing the terminal voltage deviation of the wind turbines and minimizing the output of the SVG. These are two contradictory optimization objectives. To reduce the complexity of the solving strategy and shorten the solving time, weight coefficients are employed to transform the original problem into a single-objective optimization problem, as shown in (9).

$$\begin{aligned}\min\Bigg\{&K_{\mathrm{pcc}}\left|\frac{Q_{\mathrm{SVG}}}{Q_{\mathrm{SVG}+} - Q_{\mathrm{SVG}-}}\right| \\ &+ K_{\mathrm{WT}}\frac{1}{N_{\mathrm{WT}}}\sum_{i=1}^{m}\sum_{j=1}^{n}\left(\frac{V_{\mathrm{WT}ij} - V_{\mathrm{N}ij}}{V_{\mathrm{N}ij}}\right)^2\Bigg\}\end{aligned} \tag{9}$$

where K_{pcc} and K_{WT} are the weight coefficients. These two coefficients are both nonnegative and $K_{\mathrm{pcc}} + K_{\mathrm{WT}} = 1$. Moreover, their values will affect the optimization results of the wind farm. If K_{pcc} is many times larger than K_{WT}, the optimization results may tend to the maximum reactive reserve of the SVG. At this time, the terminal voltage deviation will increase. Conversely, if K_{WT} is many times larger than K_{pcc}, the terminal voltage deviation can be restrained better, but the remaining capacity of the SVG will descend. Therefore, their values depend on the real wind farm.

Theoretically, many combinations can achieve the control objectives of (9). However, there are some other constraints in the real wind farm, such as power flow, remaining reactive power capacity, and terminal voltage. The equations for these constraints are shown as follows:

$$\begin{cases} P_{\mathrm{WT}i} - V_{\mathrm{WT}i}\sum_{j=1}^{N_i} V_{\mathrm{WT}j}(G_{\mathrm{WT}ij}\cos\theta_{\mathrm{WT}ij} \\ \quad +B_{\mathrm{WT}ij}\sin\theta_{\mathrm{WT}ij}) = 0 \\ Q_{\mathrm{WT}i} - V_{\mathrm{WT}i}\sum_{j=1}^{N_i} V_{\mathrm{WT}j}(G_{\mathrm{WT}ij}\sin\theta_{\mathrm{WT}ij} \\ \quad +B_{\mathrm{WT}ij}\cos\theta_{\mathrm{WT}ij}) = 0 \end{cases} \tag{10}$$

$$\begin{aligned} Q_{\mathrm{WT}ij\mathrm{min}} = -\sqrt{S_{\mathrm{WT}ij}^2 - P_{\mathrm{WT}ij}^2} \le Q_{\mathrm{WT}ij} \le Q_{\mathrm{WT}ij\mathrm{max}} \\ = \sqrt{S_{\mathrm{WT}ij}^2 - P_{\mathrm{WT}ij}^2} \end{aligned} \tag{11}$$

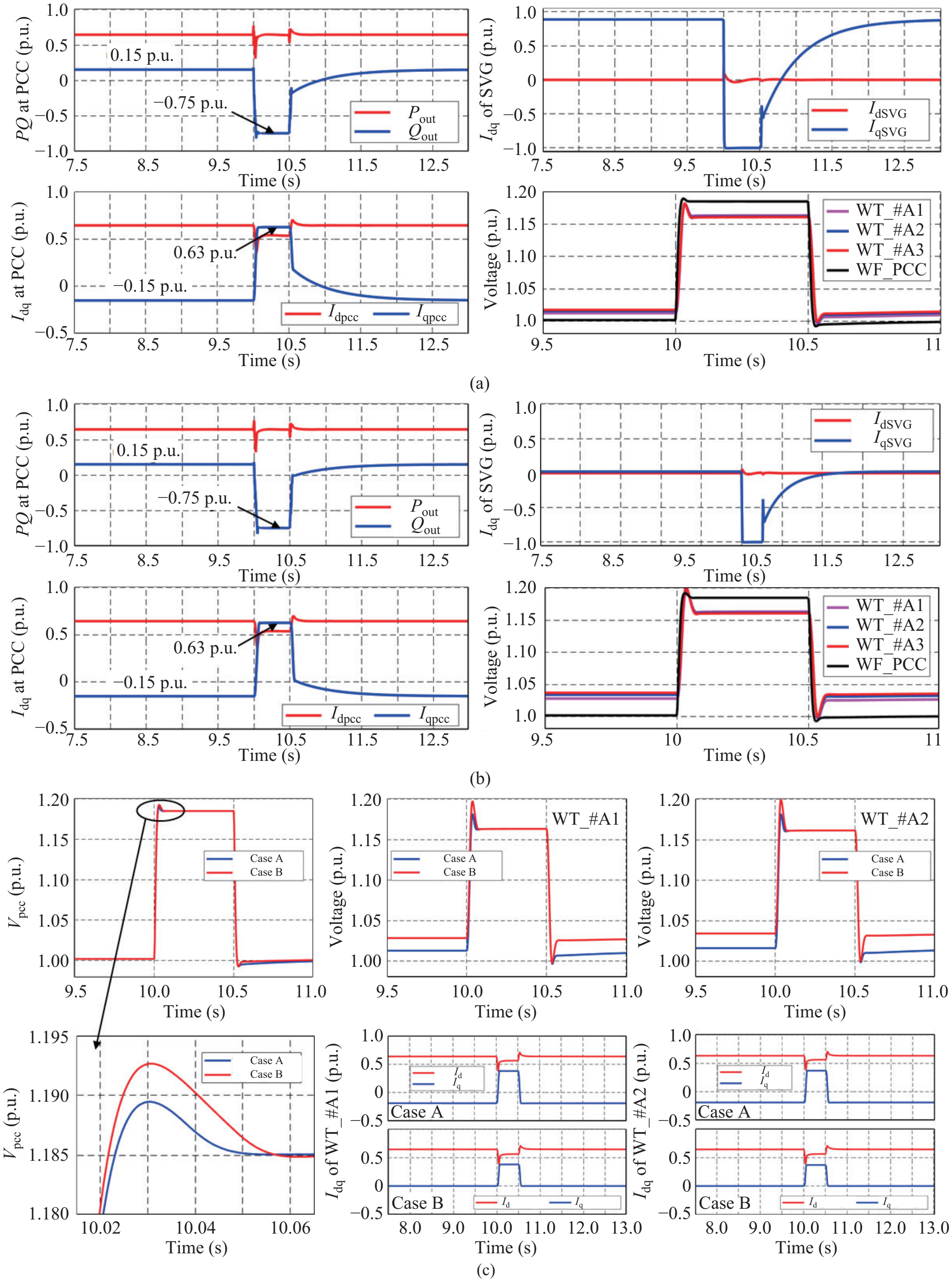

Fig. 7. Dynamic processes in different cases during HVRT. (a) Case A. (b) Case B. (c) Differences.

$$Q_{\mathrm{SVGmin}} \leq Q_{\mathrm{SVG}} \leq Q_{\mathrm{SVGmax}} \tag{12}$$

$$V_{\mathrm{WT}ij\mathrm{min}} \leq V_{\mathrm{WT}ij} \leq V_{\mathrm{WT}ij\mathrm{max}} \tag{13}$$

where $Q_{\mathrm{WT}ij\mathrm{min}}$ and $Q_{\mathrm{WT}ij\mathrm{max}}$ are the boundaries of the reactive power of the wind turbine. $V_{\mathrm{WT}ij\mathrm{min}}$ and $V_{\mathrm{WT}ij\mathrm{max}}$ are the boundaries of the terminal voltage. $G_{\mathrm{WT}ij}$ and $B_{\mathrm{WT}ij}$ are equivalent admittance and electronegativity, respectively. Equations (9) to (13) define a nonlinear optimization problem. In addition, many optimization strategies can solve this problem and obtain optimal results, such as the Particle Swarm Optimization (PSO) algorithm, and the interior point (IP) method. Given the complexity of the solving algorithm and the characteristics of nonlinear optimization, this paper employs a PSO algorithm to solve reactive power commands. The detailed solution process of PSO is illustrated in [21] and is not repeated here.

IV. CASE STUDY AND SIMULATION VERIFICATION

In this paper, two different simulation systems are designed in the MATLAB/Simulink platform to verify the improvement effect of wind farms under this RPS control method. In one case, there is only one wind farm in the selected power grid. Fig. 1 shows the structure of this wind farm. Besides, Fig. 9 illustrates the original wind speed during a certain period. Table II gives the main parameters of the wind farm and wind turbines. For other parameters, refer to [22].

A. RPS Control Strategy in a Steady State

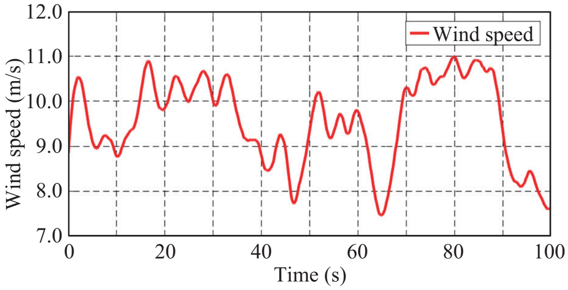

Fig. 9. Wind speed during a period.

Only Wind Farm A is connected to the selected system, and its dynamic trajectories in a steady state are shown in Figs. 10(a) and 10(b). When this RPS control strategy is not adopted, I_q of the SVG increases rapidly. Additionally, as the active power output of the wind farm increases, its maximum could exceed 0.80 p.u. According to the distribution of the terminal voltage, the maximum deviation of the terminal voltage is less than 0.03 p.u. For feeder line C in Wind

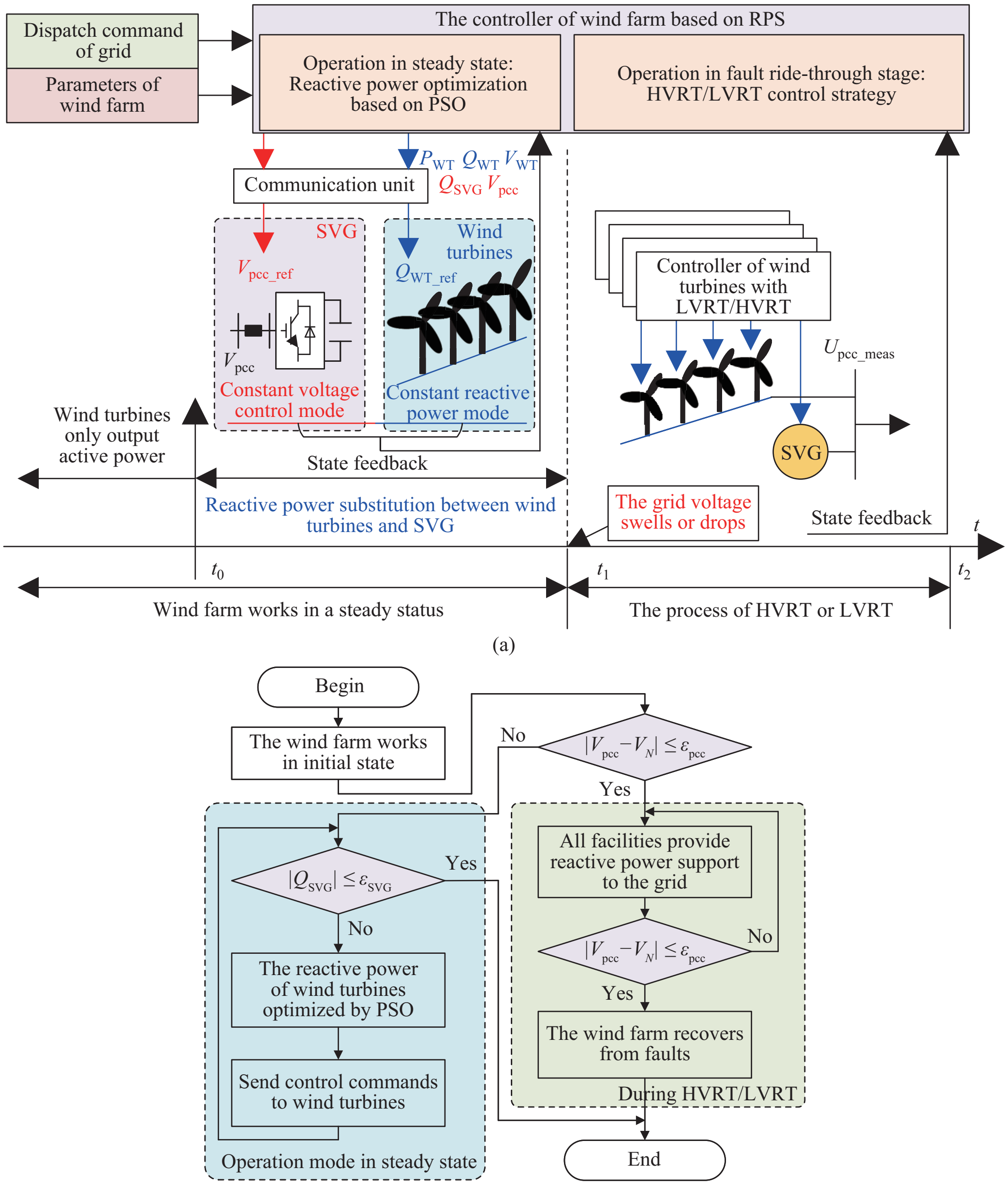

(a)

(b)

Fig. 8. RPS control strategy. (a) Its structure. (b) Its implementation process.

TABLE II
PARAMETERS OF THE WIND FARM

Variable	Description	Value
U_{N}	Voltage reference	35 kV
S_{N}	Capacity reference	1.5 MVA
Z_{Based}	Impedance reference	816.6667 Ω
U_g	Normal grid voltage	1.0 p.u.
v	Rated wind speed	12 m/s
$S_{\mathrm{N\_TBox}}$	Capacity of box transformer	1.6 MVA
$S_{\mathrm{N\_TMain}}$	Capacity of main transformer	63 MVA
$S_{\mathrm{N\_SVG}}$	Capacity of SVG	10 MVA
f_g	Fundamental frequency	50 Hz
Z_g	Grid impedance (Unit)	0.0017 + j0.0341 p.u.
$Z_{\mathrm{T\_Main}}$	Main transformer impedance	0.0016 + j0.1905 p.u.
$Z_{\mathrm{T\_Box}}$	Box transformer impedance	0.6836 + j2.0625 p.u.
Z_{Line}	Line impedance (Unit)	0.0139 + j0.0336 p.u.

TABLE III
SIMULATION RESULTS UNDER DIFFERENT WEIGHT COEFFICIENTS

Weight coefficient		Reactive power output (Mvar)		Terminal voltage (p.u.)			Remaining reactive capacity (Mvar)
K_{pcc}	K_{WT}	SVG	Wind Turbines	Max	Min	Avg	
1.00	0	1.29E-6	9.131	1.085	0.986	1.032	≈ 10
0.85	0.15	2.48E-4	8.803	1.063	1.008	1.031	≈ 10
0.75	0.25	1.19E-3	8.755	1.057	1.006	1.029	≈ 10
0.50	0.50	4.20E-3	8.675	1.047	1.007	1.028	≈ 10
0.25	0.75	0.0057	8.584	1.043	1.013	1.021	9.9943
0.15	0.85	5.8597	2.665	1.024	1.011	1.016	4.1703
0	1.00	10	−3.796	1.002	0.998	1.000	0

Farm A, since its total length is the shortest among the three feeder lines, the terminal voltage deviation of feeder line C is the smallest. For whichever feeder line, the terminal voltage deviation at the feeder terminal is always the highest.

According to Fig. 10(b), the reactive power demand is provided completely by the SVG before $t = 20$ s. When the wind turbines begin to output reactive power by employing this RPS control strategy after $t = 20$ s, I_q of the SVG decreases gradually, and even approaches zero. During this process, the active power output remains unchanged. The terminal voltage deviation does not exceed 0.05 p.u. based on the PSO algorithm. The terminal voltage at the feeder terminal is no longer the maximum value among all connected wind turbines. Furthermore, since feeder line C has the shortest distance, the wind turbines on it will provide more reactive power, so that its terminal voltage deviation is larger. However, this approach reduces the terminal voltage deviation on feeder line A significantly.

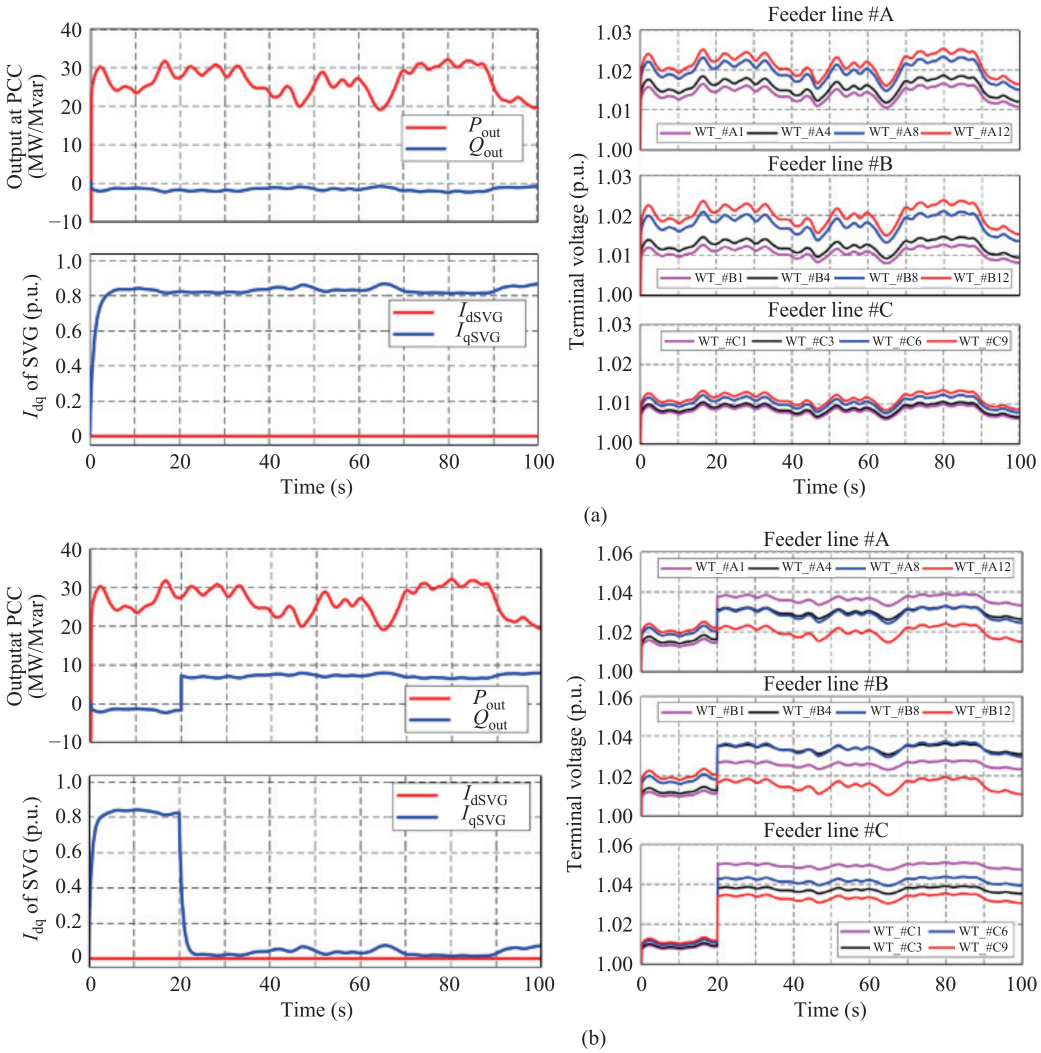

(a)

(b)

Fig. 10. Operations situation in a steady state. (a) Not adopting the RPS control strategy. (b) Adopting the RPS control strategy.

Moreover, this terminal voltage deviation between adjacent wind turbines also increases. As its total length is the shortest, the equivalent impedance is also the lowest. To reduce the terminal voltage deviation, it is advisable to utilize wind turbines located as close to PCC as possible to output reactive power. Similarly, when the active power increases as the wind speed rises, the wind farm needs more reactive power to keep $\boldsymbol{V}_{\text{pcc}}$ constant. At a result, Q_{SVG} may exceed the preset threshold. To keep the output of the SVG close to zero again, the central controller will update the operating state of each wind turbine based on PSO.

There is no unified standard for weight coefficient selection. This paper adopts several different combinations to clarify the impact of K_{pcc} and K_{WT} on the PSO algorithm. The operating state of Wind Farm A at $t = 20$ s in Fig. 9 is selected to explore this impact. As shown in Table. II, when K_{pcc} is 1, it means that there is only one optimization objective to minimize Q_{SVG}. However, the terminal voltage deviation is larger, which poses the risk of exceeding the threshold. On the other hand, when K_{WT} is 1, the terminal voltage can reach the rated voltage. However, at this time, the SVG may not have any remaining capacity. Compared to the simulation results, the operating state of the SVG is roughly the same, and the change in the terminal voltage is relatively obvious. The principle for weight coefficient selection is to minimize the terminal voltage deviation while ensuring that the output of the SVG is as small as possible. In this paper, the values of K_{pcc} and K_{WT} are 0.25 and 0.75, respectively.

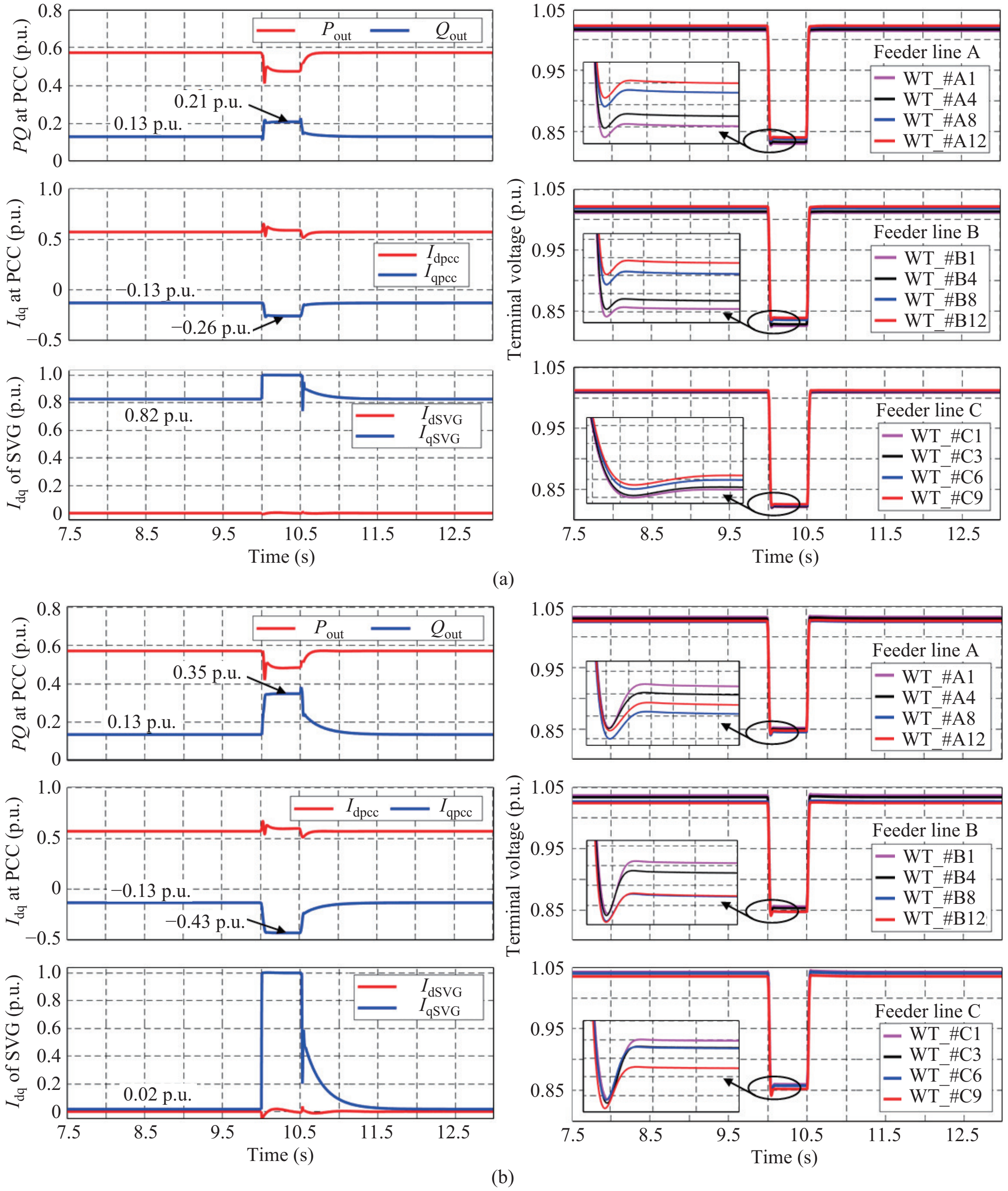

(a)

(b)

Fig. 11. Operations situation under $V_g = 0.8$ p.u. (a) Not adopting the RPS method. (b) Adopting the RPS method.

B. RPS Control Strategy During LVRT and HVRT

The wind speed at $t = 80$ s in Fig. 9 is employed as the operating state to verify the dynamic properties by adopting the RPS control strategy during the LVRT and HVRT processes. To simulate short-circuit faults in power systems, V_g is set as a drop of $t = 10$ s, and the duration of this fault is 0.5 s. The dynamic performance of this simulation system is presented in the corresponding figures.

Figure 11(a) illustrates the operating state during LVRT without using this RPS control method. Before LVRT, the wind turbines provide no reactive power and Q_{SVG} almost exceeds 0.8 p.u. When V_g drops to 0.8 p.u., the reactive current increment generated by the SVG is less. Fig. 11(b) shows the simulation results during LVRT by adopting the RPS control strategy. Before LVRT, the wind turbines bear the main reactive power demand. I_q of the SVG is close to zero. This means that the SVG can provide a reactive current increment close to 1 p.u. during LVRT.

Compared to Figs. 11(a) and 11(b), although the active power output to the grid during LVRT is the same, the reactive power output from the wind turbines with the RPS control strategy is higher than that without this control strategy. In addition, the increment rate of I_q of the SVG is different. The difference between these two factors can result in a difference in the dynamic trajectories of $\boldsymbol{V}_{\mathrm{pcc}}$ and $\boldsymbol{V}_{\mathrm{WTi}}$. According to Fig. 12(a), the partial terminal voltage curve in three feeder lines under different control strategies are compared visually. When the wind farm dose not employ this RPS control method, the voltage drop rate of wind turbine #C1 is 1.21 p.u./s, and that of wind turbine #C9 is 1.64 p.u./s. On the contrary, by adopting this RPS control method, the SVG can provide a fast and sufficient reactive current in time, the voltage drop rate of wind turbine #C1 is 0.75 p.u./s, and that of wind turbine #C9 is 1.12 p.u./s. Besides, the drop depth of the terminal voltage is also improved.

Moreover, the wind turbines provide a higher reactive current, as shown in Fig. 12(b). Since this RPS control strategy changes the operating state of the equipment before LVRT, the wind farm outputs a higher reactive current. Accordingly, the terminal voltage has been improved during LVRT.

Similarly, Fig. 13 shows the operating state of Wind Farm A when the grid voltage experiences a deep drop. Fig. 14(a) gives the comparison with the partial terminal voltage curve in feeder line A under different control strategies. According to the dynamic trajectories of these simulation results, the SVG can indeed provide fast and enough reactive power to slow down the voltage drop rate of the wind turbines. Besides, the wind turbines provide another reactive current. Then, the terminal voltage of wind turbine #A1 when the RPS control method is adopted is higher than that when the RPS control method is not adopted. In terms of system performance, when the proposed control strategy is adopted, the voltage drop rate of the wind turbines is higher, and the voltage support effect is better during LVRT.

The RPS control strategy has also been validated during the HVRT process, as shown in Figs. 15 to 17. During HVRT, the

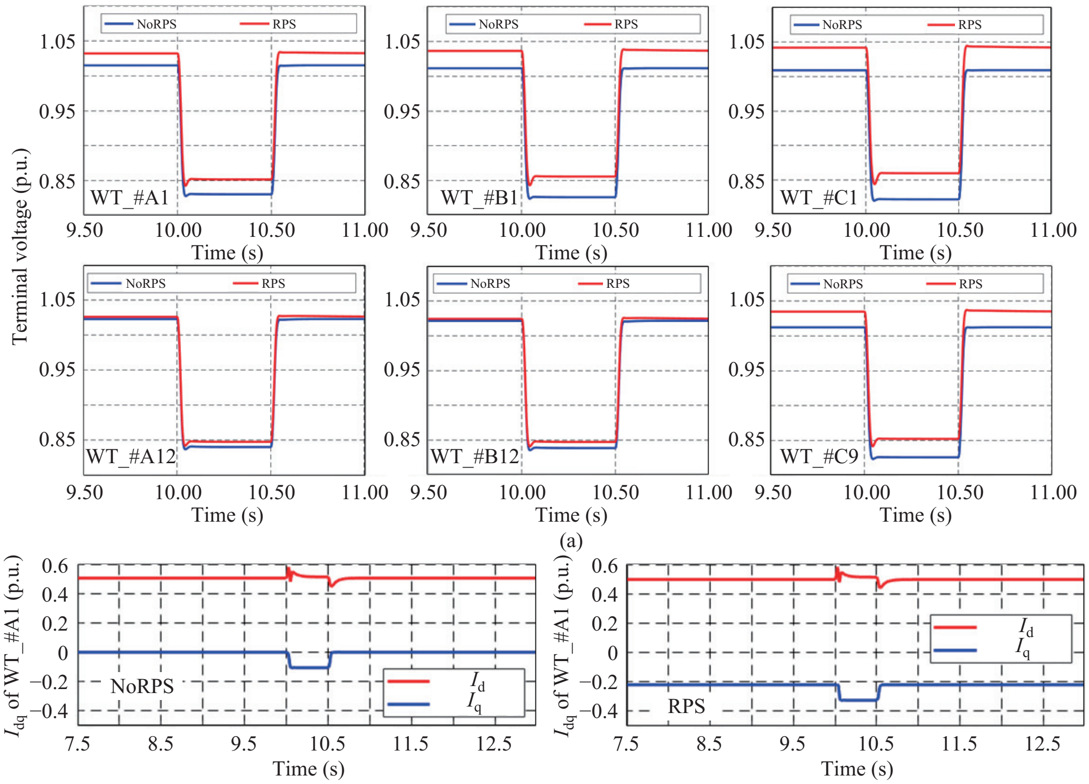

(a)

(b)

Fig. 12. Terminal voltage during $V_g = 0.8$ p.u. (a) Terminal voltage. (Note that the blue curve indicates that the RPS control strategy is not used and the red curve indicates that the RPS control strategy is adopted). (b) The dq-axis current of WT_#A1 (Note that the left figure is obtained without the RPS control strategy, and the right figure is obtained with the RPS control strategy).

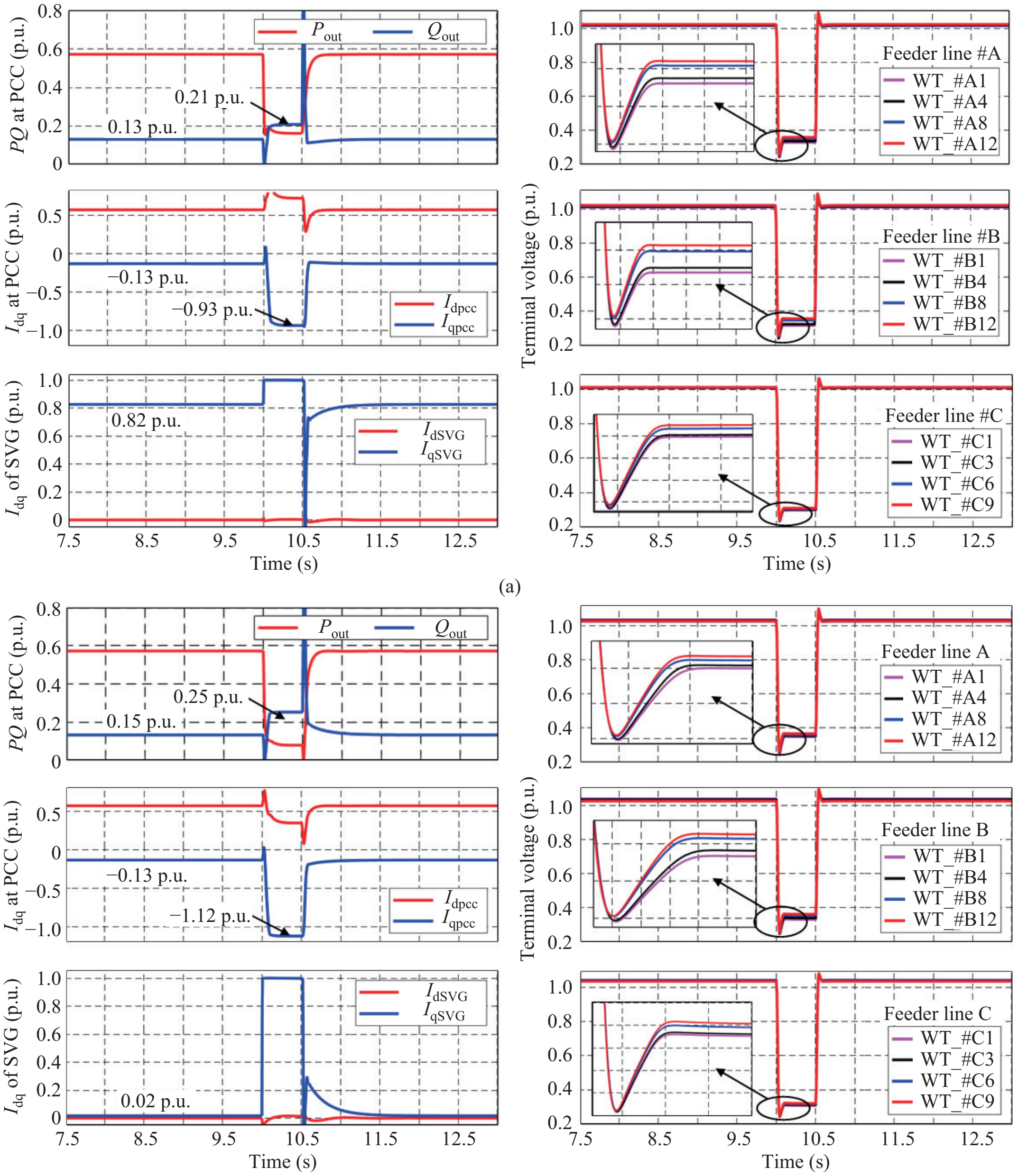

(a)

(b)

Fig. 13. Operating states under $V_g = 0.2$ p.u. (a) Without adopting the RPS control strategy. (b) Adopting the RPS control strategy.

flow direction of the reactive power is opposite. According to the dynamic trajectories of Wind Farm A, I_q of the SVG reaches -1.0 p.u. as given in Fig. 15(a). This symbol only represents the direction of reactive power flow. If this RPS control strategy is not used, the reactive current increment of the SVG can reach 1.8 p.u. Since the wind turbines do not output reactive power before HVRT, there is basically no overshoot in the terminal voltage. While in Fig. 15(b), when this RPS control strategy is adopted, the reactive current increment of the SVG is 1 p.u.

Figures 16 and 17 give the trajectories of the terminal voltage and the reactive current under different control strategies. Due to the lag in response of the wind turbines, there is significant overshoot in the voltage trajectory, and the swell rate of the terminal voltage is higher. However, the proposed RPS control method makes the wind turbines absorb more reactive power. Therefore, the amplitude of the terminal voltage has decreased. Moreover, the regulation time of the wind farm under this RPS control strategy is shorter during the stage of voltage recovery. This method can contribute to fast recovery from faults.

C. RPS Control Strategy in Regional Grid

This paper designs two wind farms connected to different buses in a regional grid system. The structure of this simulation power system is given in Fig. 18. In this case, the regional power system connects two wind farms in different buses. Besides, the wind farm adopted a single machine aggregation model with the same capacity is employed to replace the original synchronous generator. The Wind Farm A is linked to

Bus #36, and $\boldsymbol{V}_{\text{pcc}}$ is 1.025 p.u. The rated reactive capacities of SVG in Wind Farm A is 300 MVA. The other one is connected to Bus #35. It is called as "Wind Farm B", and $\boldsymbol{V}_{\text{pcc}}$ is 1.04 p.u. The rated reactive capacity of its SVG is 200 MVA.

In a steady state, the wind speed of two wind farms is the same. Fig. 19 shows the operational status of this simulation system presented in Fig. 18 under the RPS control strategy. Before this RPS control strategy is enabled, Wind Farm A outputs 650 MW, which is as high as that of Wind Farm B. In addition, Q_{SVG} in Wind Farm A is 210 Mvar, while Wind Farm B has a reactive power output of only 120 MVar from its SVG. As the wind turbines begin to generate reactive power when this RPS control strategy is enabled at $t = 10$ s, the reactive power produced by the wind turbines can serve as a substitute for that generated by the SVG, and the I_q values of the SVGs in both wind farms are close to zero. Although

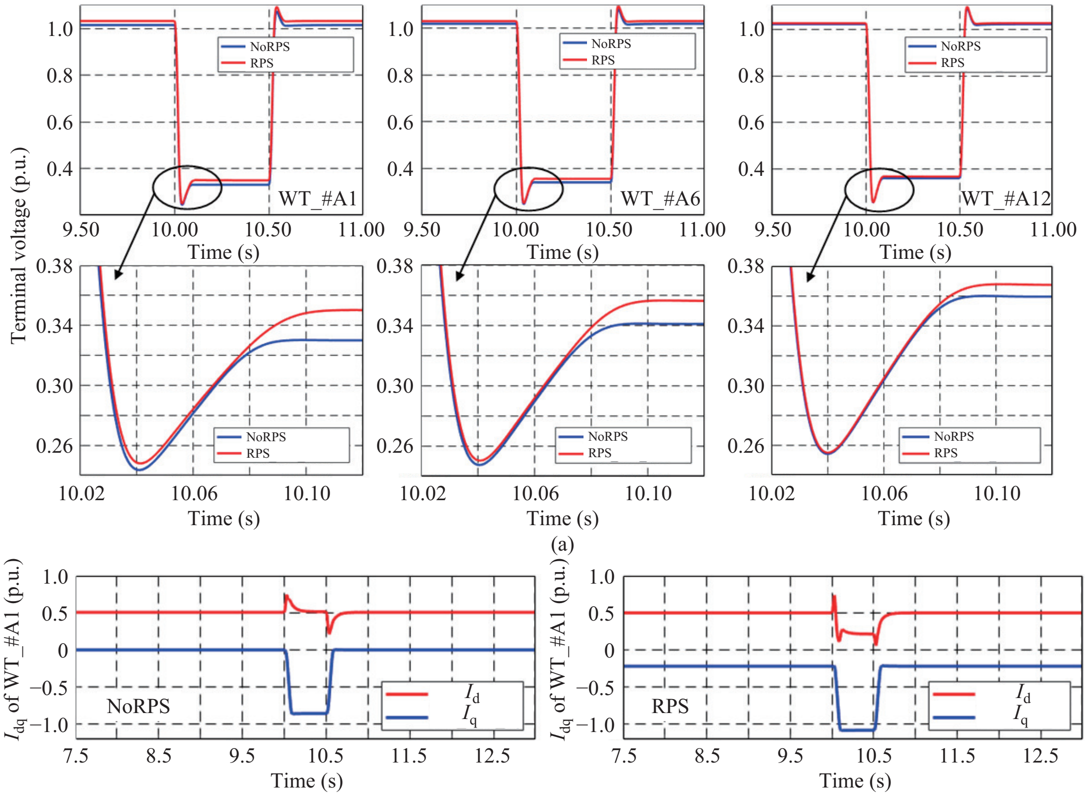

(a)

(b)

Fig. 14. Terminal voltage and its dq-axis current during $V_g = 0.2$ p.u. (a) Terminal voltage of feeder line A. (b) The dq-axis current of WT_#A1. (The left figure is obtained without the RPS control strategy, and the right figure is obtained with the RPS control strategy.).

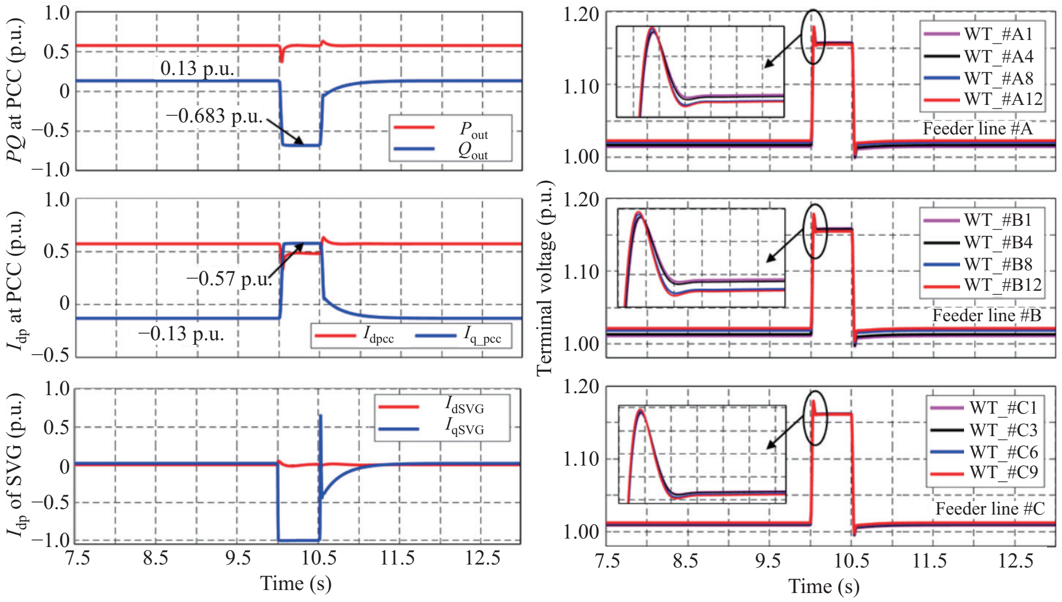

(a)

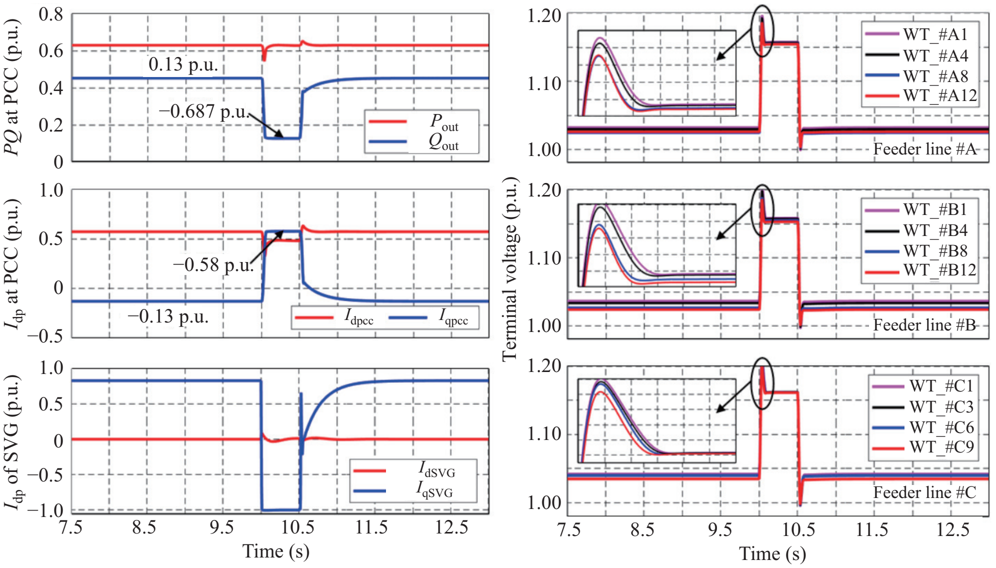

(b)

Fig. 15. Operating states under different control strategies when $\boldsymbol{V}_g = 1.2$ p.u. (a) Without adopting the RPS control strategy. (b) Adopting the RPS control strategy.

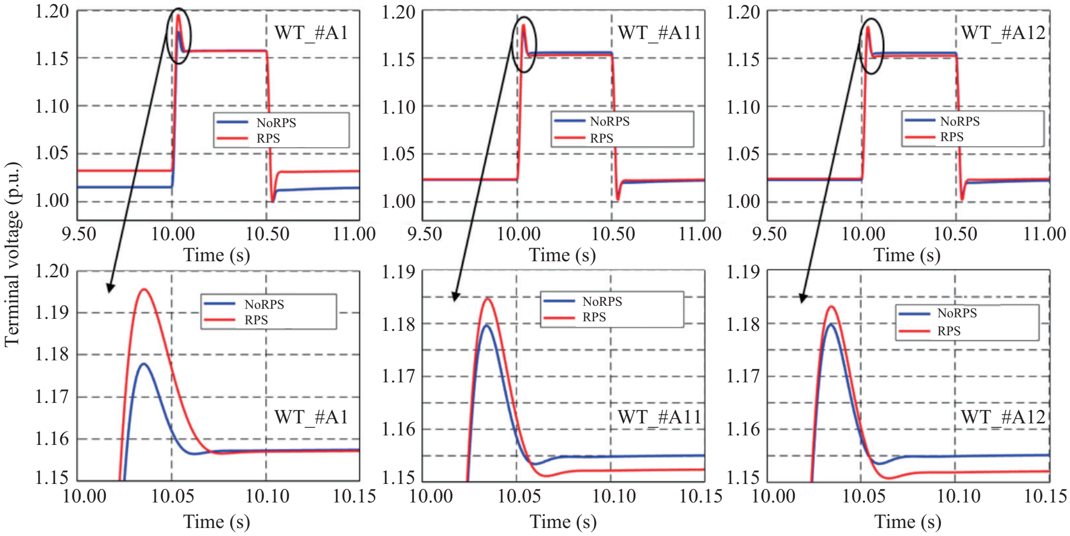

Fig. 16. Terminal voltage when $\boldsymbol{V}_g = 1.2$ p.u. The red curve indicates that the RPS control strategy is used. The blue curve indicates that the RPS control strategy is not adopted.

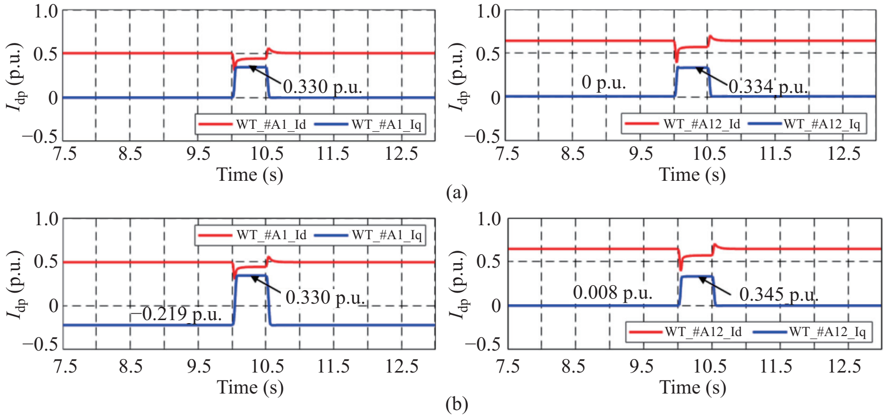

(a)

(b)

Fig. 17. dq-axis current of wind turbine #A1 and wind turbine #A12 during HVRT. (a) Without adopting the RPS control strategy. (b) Adopting the RPS control strategy.

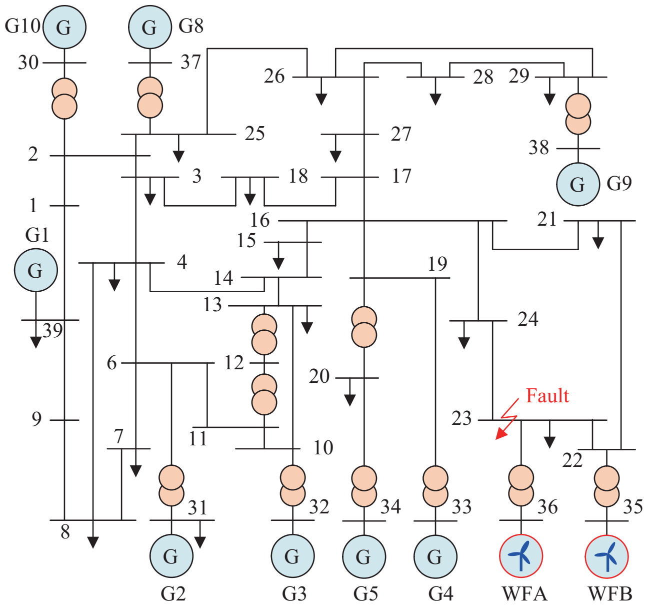

Fig. 18. Topology of the simulation system with two wind farms in this modified IEEE 39-bus System.

the active power outputs of both wind farms are the same, the impedance of the transmission line of Wind Farm B is relatively higher. For this reason, I_q of tis SVG fluctuates greatly and the terminal voltage deviation is relatively larger.

When keeping $\boldsymbol{V}_{\text{pcc}}$ constant in both wind farms, the SVG in Wind Farm A only has to provide less reactive power, resulting in a slight fluctuation in I_q of SVG. In addition, there is electrical coupling between the two wind farms through the transmission lines, and the voltage at PCC is affected slightly during the implementation of the RPS control strategy. This impact can be weakened by adding the times of reactive power substitution.

Similarly, the RPS control strategy has also been validated during the LVRT process. In a selected regional power system, Bus #23 is set to a short-circuit fault at $t = 10$ s and the duration of this fault is the same as that in Section IV-B. In addition, the operating state which is the same as that of the original system is taken to verify the dynamic performance in this case. Among them, $(P_{\text{pcc}} + \text{j}Q_{\text{pcc}})$ in Wind Farm A is (650 + j210) MVA and that in Wind Farm B is (560 + j120) MVA.

Figure 20 shows the operating states without adopting the RPS control strategy in different wind farms during LVRT. During the pre-event period, Wind Farms A and B have to abort 210 MVar and 120 MVar from the grid, respectively. Moreover, Q_{SVG} in both wind farms is greater than 0.6 p.u. This paper also demonstrates the dynamic trajectories of both wind farms by using this RPS control method during LVRT. During the pre-event stage, the q-axis currents of the SVGs in both wind farms are nearly zero. Wind Frms A and B absorb 410 MVar and 350 MVar from the grid, respectively. $\boldsymbol{V}_{\text{pcc}}$ in Wind Farm A is 0.42 p.u., but that in Wind Farm B is 0.51 p.u. The reason is that the impedances from these two wind farms to the fault point are different. Meanwhile, the wind farms enter the fault ride-through mode. The operating

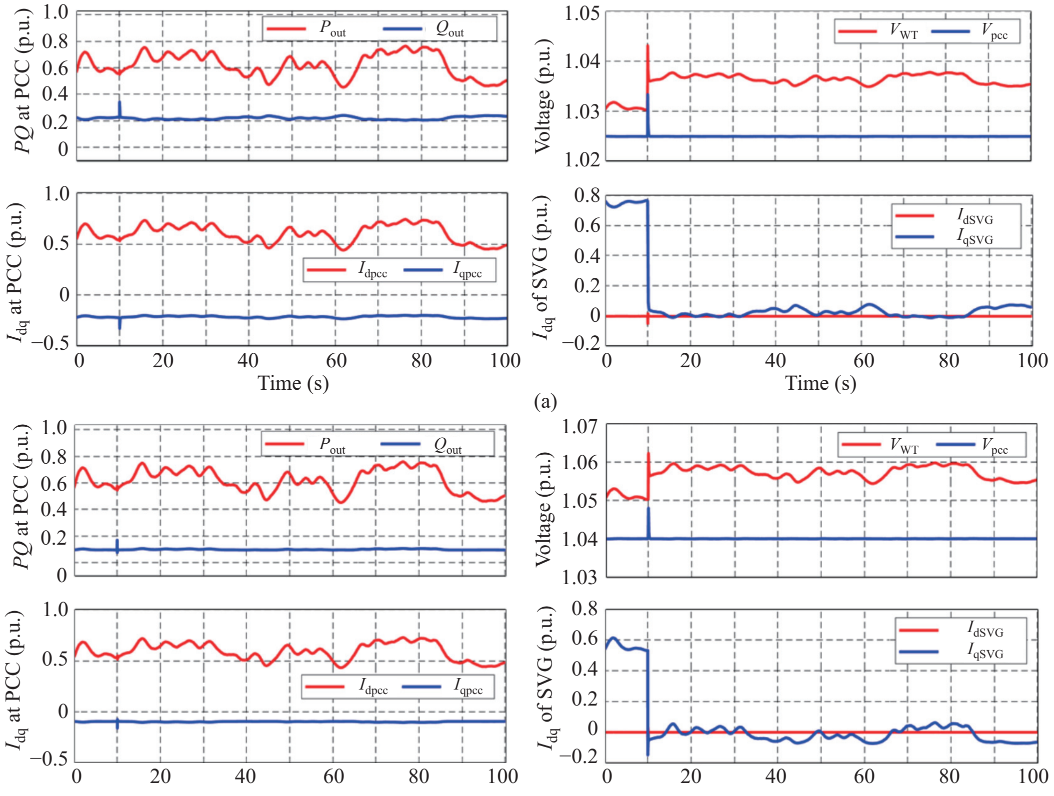

(a)

(b)

Fig. 19. Operating states of (a) Wind Farm A; and (b) Wind Farm B with adopting the RPS control strategy in a steady state.

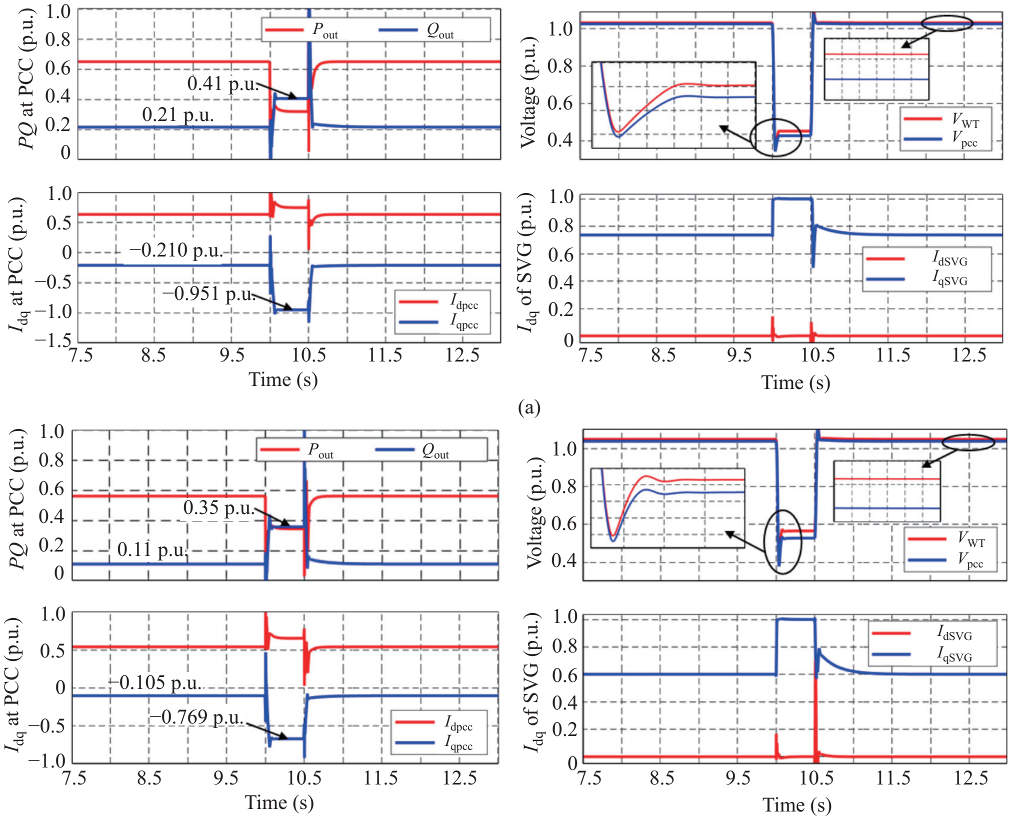

(a)

(b)

Fig. 20. Operating states of (a) Wind Farm A; and (b) Wind Farm B without adopting the RPS control strategy in the regional grid during LVRT.

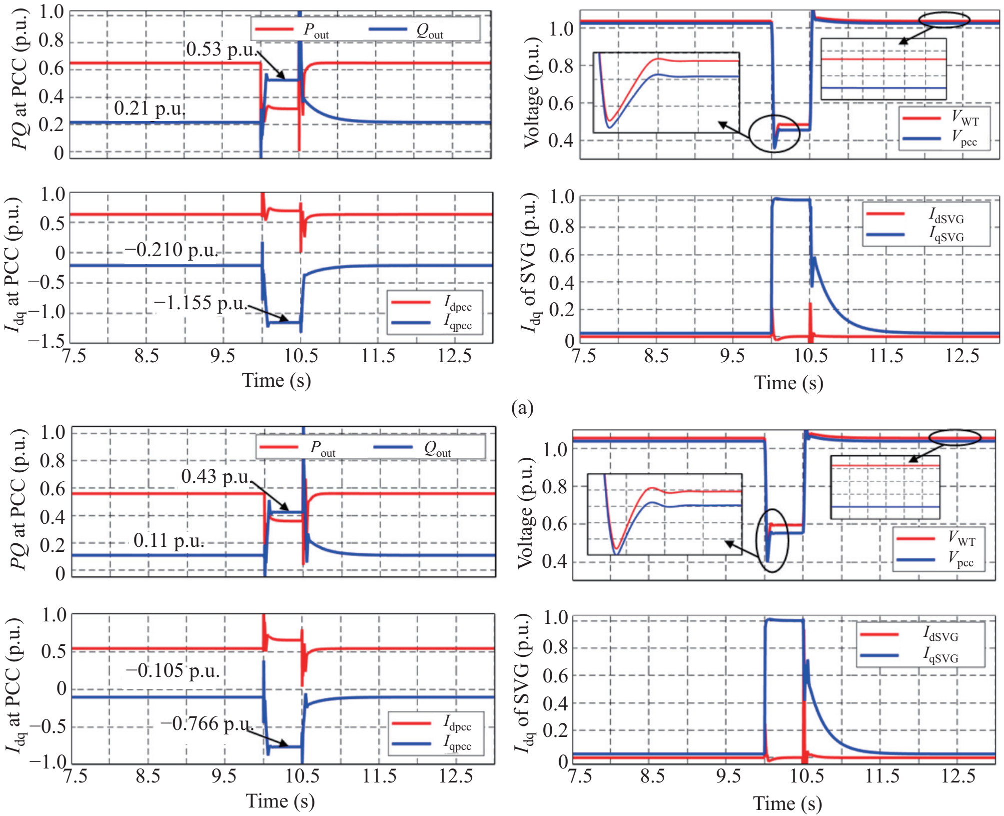

(a)

(b)

Fig. 21. Operating states of (a) Wind Farm A; and (b) Wind Farm B with adopting the RPS control strategy in the regional grid during LVRT.

states of Wind Farm B shown in Figs. 20(b) and 21(b) are similar, and the RPS control strategy can increase the reactive power increment provided by the SVG.

Figure 22 further illustrates the support capacity of this RPS control method employed at the different wind farms. As presented in Fig. 22(a), when the RPS control strategy is adopted, the drop rate of the terminal voltage in Wind Farm A is 1.45 p.u./s. Conversely, the drop rate without adopting this RPS control method is 1.95 p.u./s. The terminal voltages of the wind turbines on other feeder lines are basically similar. According to Figs. 22(a) and 22(b), this RPS control method can slow down the drop rate of the terminal voltage and increase the minimum value during fault ride-through. Compared to the simulation results during LVRT, the reactive power increment provided by the SVG with the RPS control strategy is larger than that without the RPS control strategy.

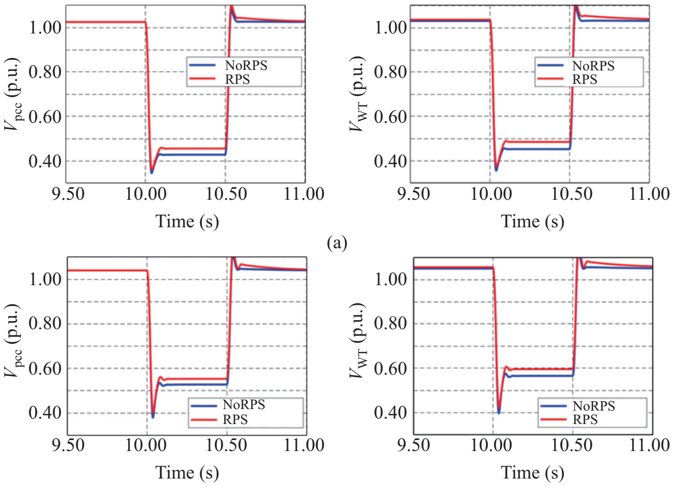

(a)

(b)

Fig. 22. Terminal voltage of (a) Wind Farm A; and (b) Wind Farm B in the regional grid.

To summarize, the results presented above demonstrate that the RPS control strategy enhances the support capacity of wind farms and improves the dynamic behavior of wind turbines.

V. CONCLUSION

This paper proposes a reactive power substitution control strategy to enhance the dynamic performance of a wind farm using a centralized control structure. The feasibility of this proposed control method is verified by building a regional power system in MATLAB/Simulink. The major conclusion of this paper is as follows.

1) For a wind farm operating under a centralized control mode, the reactive power support capacity of the SVG is superior to that of the wind turbines. Consequently, to enhance the voltage support capacity, reducing the output of the SVG in a steady state is an effective way.

2) To make the best use of the remaining capacity of the wind turbines in a steady state, the PSO algorithm is employed to make each wind turbine provide maximum RPS capacity based on its operating state and reduce its terminal voltage deviation.

3) During LVRT, this reactive power substitution control strategy can slow down the descending rate of the terminal voltage and increase its minimum value. During HVRT, this strategy can make the wind farm recover to its pre-event state more quickly. The computational pressure and communication burden of the central controller are reduced significantly.

4) This reactive power substitution control method does not change the control structure or hardware of the original wind farm, and holds significant reference in practical engineering applications.

REFERENCES

[1] P. Lakshmanan, R. J. Sun, and J. Liang, "Electrical collection systems for offshore wind farms: A review," *CSEE Journal of Power and Energy Systems*, vol. 7, no. 5, pp. 1078–1092, Sep. 2021.

[2] C. J. He, X. Q. He, H. Geng, H. D. Sun, and S. Y. Xu, "Transient stability of low-inertia power systems with inverter-based generation," *IEEE Transactions on Energy Conversion*, vol. 37, no. 4, pp. 2903–2912, Dec. 2022.

[3] W. J. Teng, X. F. Wang, Y. Q. Meng, and W. H. Shi, "An improved support vector clustering approach to dynamic aggregation of large wind farms," *CSEE Journal of Power and Energy Systems*, vol. 5, no. 2, pp. 215–223, Jun. 2019.

[4] O. P. Mahela, N. Gupta, M. Khosravy, and N. Patel, "Comprehensive overview of low voltage ride through methods of grid integrated wind generator," *IEEE Access*, vol. 7, pp. 99299–99326, Jul. 2019.

[5] *Technical Specification for Connecting Wind Farm to Power System-Part 1: On Shore Wind Power*, GB/T 19963. 1–2021, 2021.

[6] Y. F. Guo, H. L. Gao, H. Xing, Q. W. Wu, and Z. W. Lin, "Decentralized coordinated voltage control for VSC-HVDC connected wind farms based on ADMM," *IEEE Transactions on Sustainable Energy*, vol. 10, no. 2, pp. 800–810, Apr. 2019, doi: 10.1109/TSTE.2018.2848467.

[7] J. Wei, Q. W. Wu, C. B. Li, S. Huang, B. Zhou, and D. W. Chen, "Hierarchical event-triggered MPC-based coordinated control for HVRT and voltage restoration of large-scale wind farm," *IEEE Transactions on Sustainable Energy*, vol. 13, no. 3, pp. 1819–1829, Jul. 2022.

[8] Q. H. Wu, A. Bose, C. Singh, J. H. Chow, G. Mu, and Y. Z. Sun, "Control and stability of large-scale power system with highly distributed renewable energy generation: viewpoints from six aspects," *CSEE Journal of Power and Energy Systems*, vol. 9, no. 1, pp. 8–14, Jan. 2023.

[9] M. Molinas, J. A. Suul, and T. Undeland, "Low voltage ride through of wind farms with cage generators: STATCOM versus SVC," *IEEE Transactions on Power Electronics*, vol. 23, no. 3, pp. 1104–1117, May 2008, doi: 10.1109/TPEL.2008.921169.

[10] X. S. Tian, Y. N. Chi, Y. Li, H. Y. Tang, C. Liu, and Y. Y. Su, "Coordinated damping optimization control of sub-synchronous oscillation for DFIG and SVG," *CSEE Journal of Power and Energy Systems*, vol. 7, no. 1, pp. 140–149, Jan. 2021.

[11] T. Ahmed, A. Waqar, E. A. Al-Ammar, W. Ko, Y. Kim, and M. Aamir, "Energy management of a battery storage and D-STATCOM integrated power system using the fractional order sliding mode control," *CSEE Journal of Power and Energy Systems*, vol. 7, no. 5, pp. 996–1010, Sep. 2021.

[12] T. Ahmad, O. Coupiac, A. Petit, S. Guignard, N. Girard, B. Kazemtabrizi, and P. C. Matthews, "Field implementation and trial of coordinated control of wind farms," *IEEE Transactions on Sustainable Energy*, vol. 9, no. 3, pp. 1169–1176, Jul. 2018.

[13] Y. C. Wang, Y. B. Yang, and Q. S. Xu, "Reliability assessment for integrated power-gas systems considering renewable energy uncertainty and cascading effects," *CSEE Journal of Power and Energy Systems*, vol. 9, no. 3, pp. 1214–1226, May 2023.

[14] L. Guan and J. Yao, "Dynamic coupling and cooperative control for multi-paralleled doubly fed induction generator wind farms during symmetrical low voltage ride-through in a weak grid," *Protection and Control of Modern Power Systems*, vol. 9, no. 3, pp. 112–125, May 2024.

[15] M. M. Kabsha and Z. H. Rather, "Advanced LVRT control scheme for offshore wind power plant," *IEEE Transactions on Power Delivery*, vol. 36, no. 6, pp. 3893–3902, Dec. 2021.

[16] J. Wei, Y. J. Cao, Q. W. Wu, C. B. Li, S. Huang, B. Zhou, and D. Xu, "Coordinated droop control and adaptive model predictive control for enhancing HVRT and post-event recovery of large-scale wind farm," *IEEE Transactions on Sustainable Energy*, vol. 12, no. 3, pp. 1549–1560, Jul. 2021.

[17] C. P. Zhou, Z. Wang, H. H. Xin, and P. Ju, "A P-Q coordination based model predictive control for DFIG high-voltage ride through," *IEEE Transactions on Energy Conversion*, vol. 37, no. 1, pp. 254–263, Mar. 2022.

[18] X. Q. He and H. Geng, "PLL synchronization stability of grid-connected multiconverter systems," *IEEE Transactions on Industry Applications*, vol. 58, no. 1, pp. 830–842, Jan./Feb. 2022.

[19] H. Geng, L. Liu, and R. Q. Li, "Synchronization and reactive current support of PMSG-based wind farm during severe grid fault," *IEEE Transactions on Sustainable Energy*, vol. 9, no. 4, pp. 1596–1604, Oct. 2018.

[20] B. R. Karthikeya and R. J. Schütt, "Overview of wind park control strategies," *IEEE Transactions on Sustainable Energy*, vol. 5, no. 2, pp. 416–422, Apr. 2014.

[21] P. Hou, W. H. Hu, M. Soltani, and Z. Chen, "Optimized placement of wind turbines in large-scale offshore wind farm using particle swarm optimization algorithm," *IEEE Transactions on Sustainable Energy*, vol. 6, no. 4, pp. 1272–1282, Oct. 2015.

[22] Y. Y. Zhao, J. Y. Chai, and X. D. Sun, "Relative voltage control of the wind farms based on the local reactive power regulation," *Energies*, vol. 10, no 3, pp. 281, Feb. 2017.

Yuegong Li received B.S and M.S degrees in Electrical Engineering from Zhengzhou University of Light Industry, Zhengzhou, China, in 2016 and 2021, respectively. He is currently pursuing the Ph.D. degree with the Wuhan University of Technology. His current research interests include advanced control strategies and optimization algorithms on renewable power conversion systems.

Guorong Zhu received the Ph.D. degree in Electrical Engineering from the Huazhong University of Science and Technology, Wuhan, China, in 2009. From 2002 to 2005, she was a Lecturer with the School of Electrical Engineering, Wuhan University of Science and Technology. From 2009 to 2011, she was a Research Assistant/Research Associate with the Department of Electronic and Information Engineering, Hong Kong Polytechnic University, Hong Kong, China. She is currently a full Professor with the School of Automation, Wuhan University of Technology. Her research interests include wireless power transfer, the reliability of power electronics systems, and advanced control on renewable energy conversion systems.

Jianghua Lu received M.S. and Ph.D. degrees from the Wuhan University of Technology, Wuhan, China, in 2016 and 2020, respectively. From September 2018 to October 2020, he was a joint Ph.D. student funded by the China Scholarship Council with the Department of Electrical and Computer Engineering, San Diego State University, San Diego, CA, USA. He is currently a Lecturer at School of Information Science and Engineering, Wuhan University of Science and Technology. His research interests include wireless power transfer and resonant converters, and advanced control strategies on renewable power conversion systems.

Hua Geng received the B.S. degree in Electrical Engineering from Huazhong University of Science and Technology, Wuhan, China, in 2003 and the Ph.D. degree in Control Theory and Application from Tsinghua University, Beijing, China, in 2008. From 2008 to 2010, he was a Postdoctoral Research Fellow with the Department of Electrical and Computer Engineering, Ryerson University, Toronto, ON, Canada. He joined Automation Department of Tsinghua University in June 2010 and is currently a full Professor. His current research interests include advanced control on power electronics and renewable energy conversion systems, AI for energy systems. He has authored more than 300 technical publications and holds more than 30 issued Chinese/US patents. He was the recipient of IEEE PELS Sustainable Energy Systems Technical Achievement Award. He is the Editor-in-Chief of *IEEE Transactions on Sustainable Energy*. He served as general chair, track chair and session chair of several IEEE conferences. He is an IEEE Fellow and an IET Fellow, and the convener of the Modeling Working Group 8 (Modeling of Renewable Energy Generation for Power System Dynamic Analysis) in IEC SC 8A.